NASA CONTRACTOR REPORT

NASA CR-2125

NASA CR-2125

THERMAL DYNAMIC MODELING STUDY

by I. U. Ojalvo

Prepared by
GRUMMAN AEROSPACE CORPORATION
Bethpage, N.Y. 11714
for Langley Research Center

NATIONAL AERONAUTICS AND SPACE ADMINISTRATION • WASHINGTON, D. C. • OCTOBER 1972

1. Report No.	2. Government Accession No.	3. Recipient's Catalog No.
NASA CR-2125		

4. Title and Subtitle	5. Report Date
THERMAL DYNAMIC MODELING STUDY	October 1972
	6. Performing Organization Code
7. Author(s)	8. Performing Organization Report No.
I. U. Ojalvo	
9. Performing Organization Name and Address	10. Work Unit No.
Grumman Aerospace Corporation Bethpage, New York 11714	114-08-05-01
	11. Contract or Grant No.
	NAS1-10635-3
12. Sponsoring Agency Name and Address	13. Type of Report and Period Covered
National Aeronautics and Space Administration Washington, D.C. 20546	Contractor Report
	14. Sponsoring Agency Code

15. Supplementary Notes

16. Abstract

Some thermal dynamic requirements associated with the space shuttle vehicle are reviewed. Pertinent scaling laws are discussed and recommendations are offered regarding the need for conducting reduced-scale dynamic tests of major components at elevated temperatures. Items considered are the development and interpretation of thermal dynamic structural scaling laws, the identification of major related problem areas and a presentation of viable model fabrication, instrumentation, and test procedures.

17. Key Words (Suggested by Author(s))	18. Distribution Statement
Space Shuttle structural dynamics Thermal-dynamic scaling Dynamic testing	Unclassified - Unlimited

19. Security Classif. (of this report)	20. Security Classif. (of this page)	21. No. of Pages	22. Price*
Unclassified	Unclassified	72	$3.00

*For sale by the National Technical Information Service, Springfield, Virginia 22151

FOREWORD

The work reported herein was performed by the Grumman Aerospace Corporation under the NASA/Langley Master Agreement and Contract No. NAS 1-10635 for the Development and Implementation of Space Shuttle Structural Dynamics Modeling Technology. The Work Statement of Task Order No. 3, "Thermal Dynamic Modeling Study," authorized and specified the tasks to be performed in this study. The period of performance was for 12 months starting in June of 1971.

The overall supervision of programs under the Master Agreement is provided by Mr. E. F. Baird, Master Agreement Program Manager. Dr. I. U. Ojalvo was the Task Order No. 3 Project Manager and principal author of this report. Many individuals at Grumman contributed to the work reported here. The author, however, wishes to specifically acknowledge the efforts of Dr. Ernesto Saleme for assisting in the derivation of the thermal scaling laws, Mr. Eric Powell for effecting the scale model design, Messrs. Paul Bell and Frank Altieri for performing the structural analyses, and Messrs. Vincent Iaccono and E. Lee for conducting the thermal analyses. He is also grateful to Dr. Warner Lansing for his advice and many useful suggestions.

Page Intentionally Left Blank

CONTENTS

CONTENTS (Cont)

ILLUSTRATIONS

TABLES

NOMENCLATURE

A	Cross-sectional area
D	Plate or shell stiffness
E	Modulus of elasticity
$\overline{F}$	Defined on page
G	Shear modulus
$H(\omega)$	Fourier Transform of $\overline{h}(t)$
I	Beam moment of inertia
L	Length (physical or characteristic)
M	Beam moment
N	Beam force
T	Temperature; referred to room temperature or absolute zero
V	Volume
c	Specific heat
f	Vibration frequency
g	Gravity or body-force field
h	Convective film coefficient
$\overline{h}(t)$	Transient structural displacement
i	Square root of -1
k	Conductivity coefficient
$\dot{q}$	Incident heat flux
r	Radius coordinate; measured from center-of-twist
t	Time
u,v,w	Displacement components
x,y,z	Position coordinates
α	Coefficient of thermal expansion
δ_{ik}	Kronecker delta
ϵ	Strain
ε	Emissivity
θ	Temperature scale; see Eq. 3
λ	Length scale; see Eq. 4
υ	Poisson's ratio
ρ	Mass density

σ	Stress
$\bar{\sigma}$	Stephen Boltzmann constant
τ	Time scale; see Eq. 3
$\{\phi\}$	Modal vector
ω	Circular frequency

Subscripts refer to the following quantities

A	Area
H	Heated
L	Length
O	Room Temperature
T	Thermal
V	Volume
c	Conduction
i,j,k	Node points or coordinate directions
m,n,r,s	Node points
s	Surface
t	Time
u,v,w	Displacements
x,y,z	Cartesian coordinates
eff	Effective
1000, 1200	Temperatures in degrees Fahrenheit

Superscripts

$(\ )^k$	Refers to mode number
$\bar{(\ )}$	Implies averaging, except as noted above for $\bar{F}$, $\bar{h}(t)$ and $\bar{\sigma}$
$(\ )'$	Refers to model

THERMAL DYNAMIC MODELING STUDY

by I. U. Ojalvo

Grumman Aerospace Corporation

SECTION 1 INTRODUCTION AND SUMMARY

The space shuttle thermal design must accommodate the environments associated with prelaunch cooling, boosted flight, earth orbit operation, reentry, and postlanding soak-back. The design conditions which are believed to be of importance to the shuttle's thermal-structural response are:

- Reentry - which will establish the most severe thermal environment, thus designing most of the thermal protection system (TPS) and causing the greatest primary-structure thermal stresses
- Abort maneuvers - during flight these are of less importance because of the present decision to define an "admissible" abort as one which a reentry based design could survive. Pad aborts, however, in which the orbiter accelerates away from a booster which is about to explode, are concerned with tradeoffs between high separation acceleration loads, and thermal-dynamic loads resulting from such an explosion
- Stage separation - engine firing of one vehicle in close proximity to portions of another vehicle's structure, such as a fin, could cause high local thermal stresses. This, of course, is highly dependent upon the structural configuration of the mated vehicles and fuel tanks
- Orbital environment - the vehicle temperature prior to reentry strongly governs its internal temperature during reentry. It is possible that different relative solar positions, prior to reentry, could account for significantly different thermal states

Requirements associated with the above phases present a wide range of formidable thermal-dynamic structural problems. Although related analysis procedures have improved significantly in the past decade, analytical difficulties still exist due to geometric nonlinearities, inelastic and nonlinear material behavior, complex liquid-solid interactions, and the presence of poorly defined damping mechanisms. Thus, analytical solutions must be supported by carefully controlled laboratory tests. Furthermore, the large size of the vehicles involved requires that much of the

experimental work be performed on reduced-scale models. However, before meaningful tests can be conducted, it is necessary to understand the proper thermal dynamic similarity laws and to evaluate the feasibility of their implementation in a practical modeling program. The present work is directed towards providing basic information for designing the models and conducting the required tests. Items considered are the development and interpretation of thermal dynamic structural scaling laws, the identification of major related problem areas, and the presentation of viable model fabrication, instrumentation, and test procedures.

A device employed to aid this general study was the selection of a particular component -- an orbiter fin -- to serve as a focal point for portions of this effort. Thermal structural and stiffness analyses were performed upon the fin for a typical reentry maneuver and for a 1/10th reduced scale replica model of it. In addition, manufacture, test, and cost analyses were also performed upon the fin model.

Thermal and structural dynamic similarity laws are derived and interpreted in Section 2 with regard to general shuttle design concepts. It is shown that the major difficulty associated with application of the scaling laws is that the internal radiation, convection and conduction modes of heat transfer do not scale uniformly on a reduced scale replica model. For example, the ratio of model to prototype time-scale is proportional to length-ratio squared for conduction, but length-ratio to the first power for radiation and convection. A second difficulty is that, compared to the prototype, the model time-scale may shrink so substantially as to preclude the use of conventional steady-state vibration testing.

Model design of the orbiter fin selected for detail consideration is reported in Section 3. Geometric distortions, consistent with practical manufacturing requirements, are discussed. Results of the study indicate the feasibility of replica model manufacture but underscore its extremely high cost.

Temperature, stress and stiffness analyses for the fin and its model undergoing a reentry maneuver are presented in Section 4. Geometric distortion and replica size-scaling errors in the model are quantitatively evaluated and found to be small. Furthermore, it is demonstrated that thermal stresses may be greatly relieved through implementation of intelligent design concepts. In particular, for the case studied it is shown that the use of corrugated (as opposed to noncorrugated) spar webs reduces primary thermal stresses dramatically. Thus, reductions in

cross-sectional twisting stiffnesses (up to 8%) were not influenced by destabilizing thermal stresses, but were due almost entirely to reductions in material stiffness properties associated with the elevated temperatures.

Dynamic testing at elevated transient temperatures is discussed in Section 5. Such items as experimental methods, instrumentation, excitation methods available, and necessary data processing techniques are identified.

Concluding remarks are presented in Section 6. Recommendations are offered regarding the need for conducting reduced-scale dynamic tests of major structural components at elevated temperatures, including practical suggestions for implementing such tests.

It is hoped that the present "paper-study" will alert the aerospace community to some important aspects associated, with not only shuttle-related models, but with heated structural models in general. Another goal is that this effort provide useful information towards planning meaningful thermal dynamic experiments. It is strongly felt, however, that only through careful experiments, with actual full-scale and model hardware, will a true appreciation of the need for such tests become evident.

Page Intentionally Left Blank

SECTION 2 SCALING LAWS

A number of works on general modeling laws, structural dynamic similitude, or thermal scaling alone have been presented, several of which are included in References 1 through 3. The present work differs from these, however, in that an attempt is made to identify and interpret the relevant thermal dynamic scaling laws as they apply to space shuttle primary structure. Also included is an investigation into the importance and feasibility of their application in a practical modeling program.

The basic dimensionless groups for thermal dynamic model studies of aircraft and spacecraft structures are derived from equations governing internal heat transfer and structural dynamic response. Although other derivation procedures are available, this method is preferred since it provides more insight than the mere knowledge of the dimensionless variables entering the problem.

After deriving rather general scaling laws between model and prototype, they are specialized for application to space shuttle primary load-carrying structure. Parameters associated with the possible use of different temperatures, materials, and method of construction between the prototype and the model are also discussed in light of an approximately 1/10th reduced-scale model.

Although the aerodynamic environment of the shuttle prototype is the primary source of heating, the possibility of testing a 1/10th scale model in a high stagnation temperature wind tunnel is not likely because of the great expense required to develop such a facility. In connection with this, it is noted that the similarity laws for complete aerothermoelastic testing were investigated by Dugundji and Colligeros (Reference 4), who found that similitude in the general case was difficult to achieve for a scale ratio other than unity. Their conclusions suggest the use of "incomplete aerothermoelastic testing" and "restricted purpose" models. For practical reasons it is anticipated that model heating would be best accomplished by the use of quartz lamps programmed to generate predetermined temperature-time profiles at selected points instrumented with thermocouples. Also, since the thermal protection system (TPS) will not be part of the load carrying structure, only TPS backface temperatures

and TPS mass need be simulated, thus simplifying model fabrication and lowering test temperature levels.

2.1 THERMAL SCALING LAWS

2.1.1 Derivation

The mechanisms of internal heat transfer which may be present simultaneously are: conduction, convection, and radiation. Combining these into a single term ($\dot{q}$), defined as the rate of heat absorbed by a body, and applying the first law of thermodynamics (conservation of energy), yields:

$$\rho c \, V \frac{\partial T}{\partial t} = \dot{q} \tag{1}$$

where ρ, c, V and T, respectively, are the density, specific heat, volume, and temperature of the body, and t is time.

Applying Eq. 1 to a given element i of a lumped thermal node idealization, and expanding the right-hand side explicitly into its various components, results in the internal heat balance equation:

$$\rho_i c_i V_i \frac{\partial T_i}{\partial t} = \underbrace{\sum_m k_{im} \frac{A_{im}}{L_{im}} (T_m - T_i)}_{\text{(conduction)}} + \underbrace{\sum_n h_{in} A_{in} (T_n - T_i)}_{\text{(convection)}}$$

$$+ \underbrace{\sum_r \bar{\sigma} A_{ir} \bar{F}_{ir} (T_r^4 - T_i^4)}_{\text{(radiation)}} + \underbrace{\sum_s \dot{q}_{is} A_{is}}_{\text{(heat flux source)}} \tag{2}$$

The specific form used in Eq. 2 is not unique, but represents the formulation typically programmed and employed for complex structural temperature analyses. The variables involved are defined as follows:

k_{im}, L_{im}, A_{im}	are the conductivity coefficient, length and area, respectively, of the heat conduction path joining elements i and m
h_{in}, A_{in}	are the convective film coefficient and the surface area, respectively, between elements i and n
$\bar{\sigma}$	is the Stephan-Boltzmann constant

A_{ir} is the surface area of element i that "sees" element r

$\bar{F}_{ir}$ is a radiation heat transfer coefficient which depends on the geometry and surface emissivities of the structure

$\dot{q}_{is}$ is an additional heat flux rate associated with boundary-condition nodes

A_{is} is the nodal surface area through which additional heat flux passes to element i

T_i, T_m, T_n, T_r are absolute temperatures

The temperature and thermal time scales, θ and τ_T, respectively, are defined by the ratios

$$\theta = \frac{T'}{T} \quad \text{and} \quad \tau_T = \frac{t'}{t} \tag{3}$$

where the primed quantities refer to model quantities*, and the length, area and volume scales are defined as follows:

$$\lambda_L = \frac{L'}{L}, \quad \lambda_A = \sqrt{\frac{A'}{A}} \quad \text{and} \quad \lambda_V = \sqrt[3]{\frac{V'}{V}} \tag{4}$$

Subscripts are used on each λ to accommodate the possibility of employing distorted, as opposed to geometrically replica, models. For the case of replica model scaling, it is obvious that the L, A, and V subscripted length-ratios are all equal.

Applying Eq. 2 to both prototype and model structure, employing Eq. 3 and 4, and comparing the results yields the following scaling laws to maintain the same scaled temperature-time profile in both:

(conduction) $$\frac{k}{\rho c} = \frac{k'}{\rho' c'} \frac{\tau_T \lambda_{Ac}^2}{\lambda_L \lambda_V^3} \tag{5}$$

(Cont. on following page)

(convection) $$\frac{h}{\rho c} = \frac{h'}{\rho' c'} \frac{\tau_T \lambda_{As}^2}{\lambda_V^3}$$

---

*A distinction is made between thermal time scale (τ_T) and structural dynamic time scale (to be introduced in section 2.2 as τ_D) since thermal events occur at a much slower rate than vibratory mechanical events for the problems under consideration. Thus, for engineering analysis purposes, thermal states may be assumed quasi-static with regard to dynamic response, which for modeling purposes implies that τ_T may be selected independent of τ_D.

(radiation) $$\frac{F}{\rho c} = \frac{F'}{\rho' c'} \frac{\tau_T \theta^3 \lambda_{As}^2}{\lambda_V^3} \qquad (5)$$

(heat flux) $$\frac{\dot{q}}{\rho c} = \frac{\dot{q}'}{\rho' c'} \frac{\tau_T \lambda_{As}^2}{\lambda_V^3 \theta}$$

(Cont. from previous page)

where primes over quantities refer to model parameters, and indices im, ir and is have been eliminated for simplicity. However, subscripts c and s have been added to the λ_A^2 to denote scaled area ratios associated with heat transfer through either a cross-sectional or surface area, respectively. Combining Eq 5, and using Eq. 3 and 4 yields the dimensionless groups

$$\frac{kt}{\rho c L^2}, \quad \frac{ht}{\rho c L}, \quad \frac{\bar{\sigma} \bar{F} t T^3}{\rho c L} \quad \text{and} \quad \frac{\dot{q} t}{\rho c L T} \qquad (6)$$

where the Stefan-Boltzman constant, $\bar{\sigma}$, and the absolute temperature, T, have been introduced to make the last two groups dimensionless, and L is a characteristic length (not necessarily a physical distance between two points). The first of these dimensionless groups is the Fourier Number, while the second and third are products of the Fourier Number with the Biot and Stefan numbers, respectively (Reference 5).

2.1.2 Interpretation

It can easily be seen that if the model is a geometrical replica, is made of the same material, has the same surface finish and heat flux rate as the prototype, and internal convection coefficients are identical, it will not be possible to satisfy all the requirements for any length-scale other than unity since Eq. 5 becomes:

$$\begin{aligned} &\text{(conduction)} && \tau_T = \lambda^2 \\ &\text{(convection)} && \tau_T = \lambda \\ &\text{(radiation)} && \tau_T = \lambda/\theta^3 \\ &\text{(heat flux)} && \tau_T = \lambda\theta \end{aligned} \qquad (7)$$

whose only nontrivial solution* is

$$\lambda = \tau_T = \theta = 1 \qquad (8)$$

---

*The trivial solution referred to is $\lambda = \tau_T = 0$, which is not physically useful.

If conductive heat transfer does not enter into the problem (or can be disregarded because it is small) the first of Eq. 7 need not be satisfied and the remaining two admit the solution

$$\lambda = \tau_T \quad \text{and} \quad \theta = 1 \tag{9}$$

However, if conduction is the only mode of heat transfer to be considered, then only the first of Eq.7 need be satisfied.

It should be noted that, the specific heat, c, and density, ρ, are material properties while the convective film coefficient, h, and the radiation coefficient, $\overline{F}$, depend upon other characteristics such as surface roughness, and surface coating. Although the conductivity is also a material property, the conductivity coefficient, k, may refer to an overall conductive path and include such considerations as joint conductivity, which is obviously a function of the type of joint.

It may then be possible, even when using geometric scaling and the same material and temperatures for model and prototype, to satisfy all the requirements of Eq.5 (if not exactly, then with sufficient approximation) by making the model in such a way that:

$$\frac{k'}{k} = \frac{\lambda^2}{\tau_T}$$

$$\frac{h'}{h} = \frac{\overline{F}'}{F} = \frac{\dot{q}'}{\dot{q}} = \frac{\lambda}{\tau_T} \tag{10}$$

It should be noted that in all probability there will be difficulty in geometrically scaling all member dimensions accurately (such as the cross-section of a thin post). In such cases, reference must be made to Eq. 4 and 5 to identify the pertinent physical dimensionless ratios so as to evaluate any distortions introduced by the model.

The basic conflict in accurately modeling all internal modes of heat transfer, as applied to shuttle primary structure, may be investigated in a preliminary way as follows. For discussion purposes only, consider the problem of modeling a wing with approximately 0.9 m (3 ft) between upper and lower titanium covers, 315°C (600°F) bottom-side and 204°C (400° F) top-side temperatures and negligible chord and spanwise thermal gradients.

The black-body radiation flux corresponding to 315°C and 204°C (600°F and 400°F) is about 10 and 4 $\frac{\text{g-cal}}{\text{cm}^2\text{-min}}$ (2200 and 940 Btu/hr-ft^2), respectively. If hot and cold regions can "view" each other, net radiant flux levels will be of the order of 6 $\frac{\text{g-cal}}{\text{cm}^2\text{-min}}$ (10^3 Btu/hr-ft^2). By comparison, the conduction heat transfer for a gradient of 111C° over a 0.9m (200F° over 3 ft) distance for titanium at a wing area density of 1 gm/cm^2 (2lb/ft^2) would only be on the order of 0.006 $\frac{\text{g-cal}}{\text{cm}^2\text{-min}}$ (1 Btu/hr-ft^2) (it can also be shown that internal natural convection effects for this case are also small). Hence, the principal influence on the structural temperature distribution would be the net radiant flux. Moreover, since the structural elements, exclusive of any honeycomb construction, have relatively thin gages (say 0.6 cm (1/4 in.) maximum for the prototype), it can be shown that the temperature variation within an element will be small across its thickness. Therefore, it appears reasonable to neglect transient conduction considerations in a first approximation to thermal modeling and select $\tau = \lambda$ as the appropriate time scale.

A similar result was obtained for an ablator or reusable surface insulation (RSI) protected aluminum wing using a 48 node thermal model (see Fig. 1) with ablator backface heating rates shown in Fig. 2. Runs were made for the prototype and a 1/10th scale replica model. Results for nodes 1 and 11 (Fig. 1) are plotted in Fig. 3. They reveal peak temperature differences of 85C° (150F°) and maximum thermal scaling errors of only 8.5C° (15F°). Greater scaling errors occur, however, for nodes with larger conduction couplings. The largest discrepancy encountered with the present idealization was 28C° (50F°), which occurred at node 35 (Fig. 1 and 4). It is felt that the errors indicated for this node are overly conservative (i.e., they appear higher than they really would be in an actual test) as the mass concentration used was high and all radiation couplings to this node were neglected. Nevertheless, the overall results are consistent with what might be expected when dealing with lower structural temperatures and higher material conductivities. Both of these factors tend to increase the ratio of conduction to radiation heat transfer, thus causing greater, but acceptable, modeling distortions.

A more detailed thermal analysis upon a high temperature alloy structure without a TPS is presented in Section 4.1. As might be anticipated, the percentage errors associated with it are lower because the ratio of radiation to conduction is even higher than the two cases discussed previously.

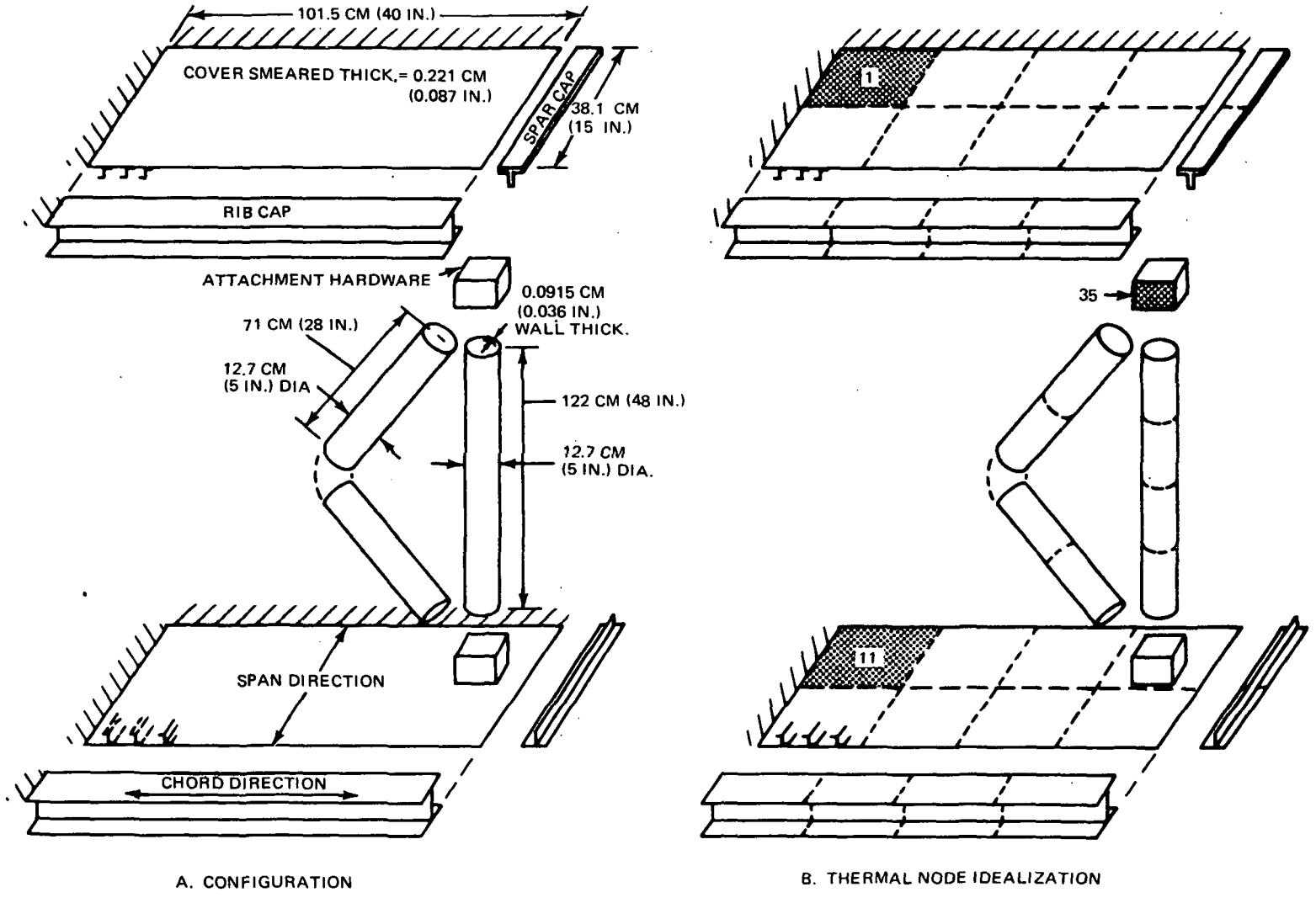

Fig. 1 Thermal Model of an RSI Protected Aluminum Shuttle Wing-Segment

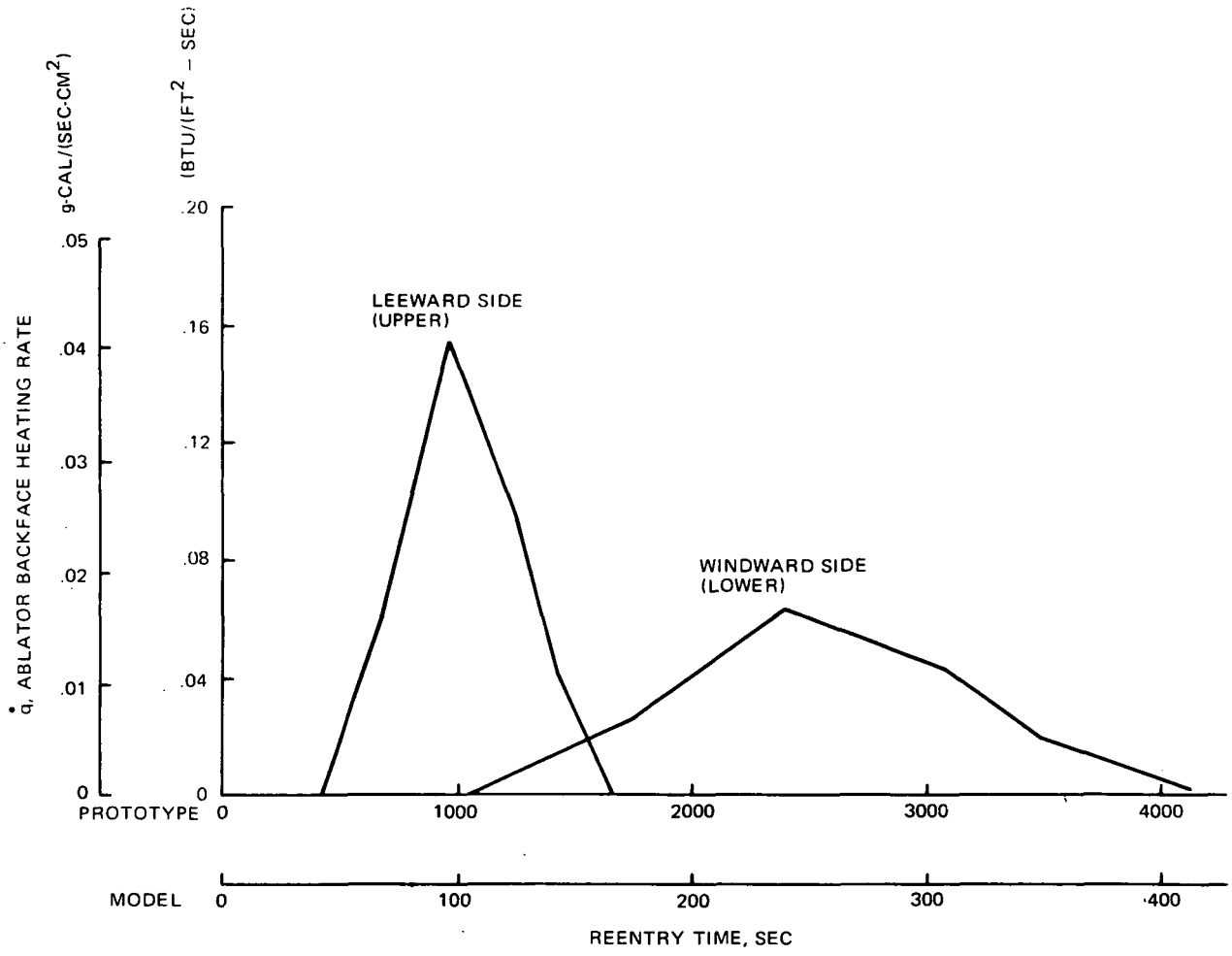

Fig. 2 RSI Backface Heating Rates Used for Aluminum Shuttle Wing Thermal Model

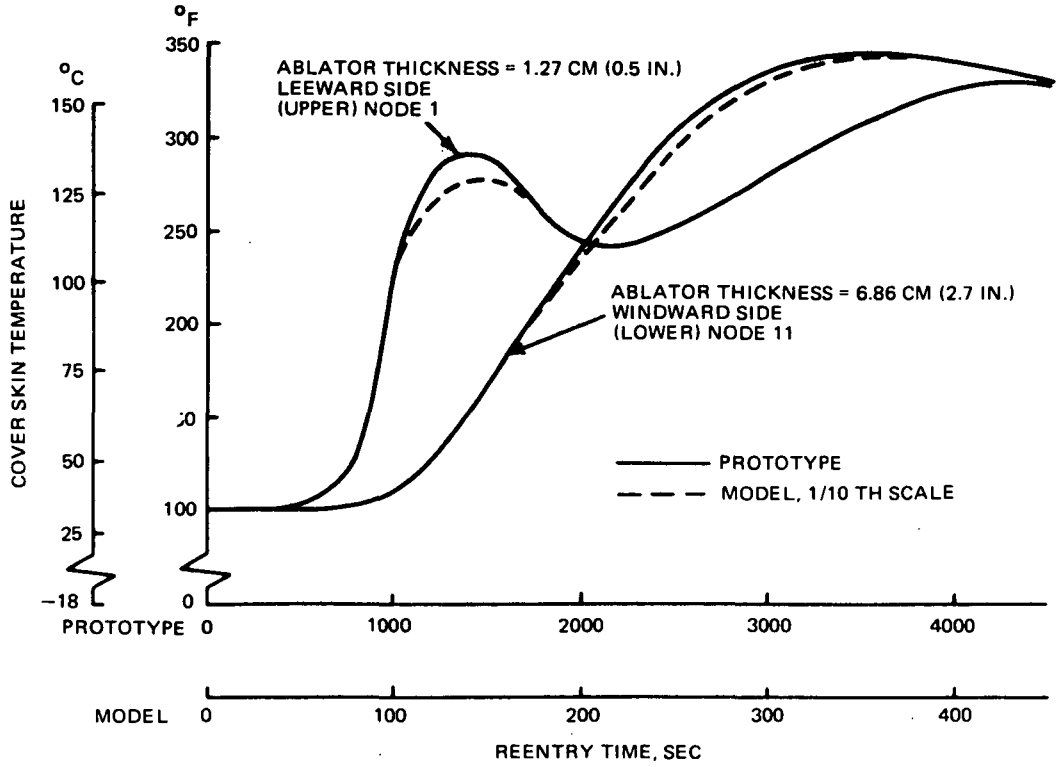

Fig. 3 Comparison of Shuttle Wing-Segment Skin Temperatures for Aluminum Prototype and 1/10th Scale Aluminum Model

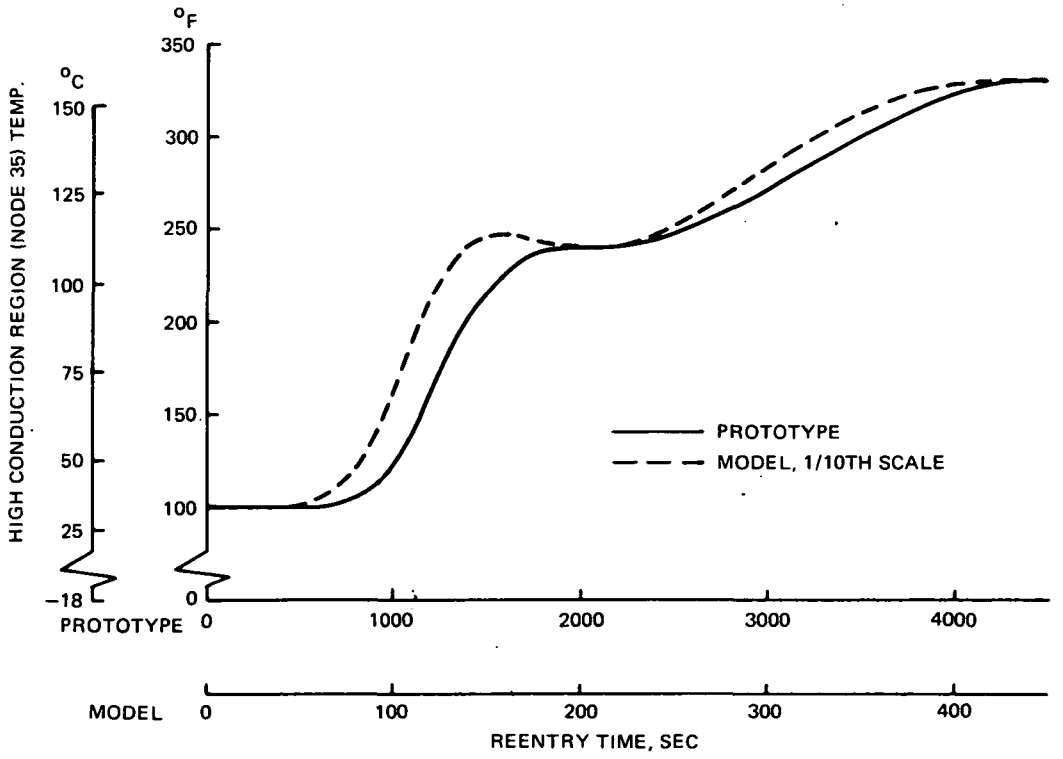

Fig. 4 Comparison of Shuttle Wing Hardware-Attachment-Point Temperatures for Prototype and 1/10th Scale Model

2.2 STRUCTURAL DYNAMIC SCALING LAWS

2.2.1 Derivation

Elasticity equations governing the stresses and large deflections in a three-dimensional, isotropic, heated body which obeys Hook's law can be written in indicial tensor form as

$$\frac{\partial \sigma_{jk}}{\partial x_k} = \rho \frac{\partial^2 u_j}{\partial t^2} - \rho g_j \qquad j, k = 1, 2, 3 \tag{11}$$

and

$$\epsilon_{jk} = 1/2\left(\frac{\partial u_j}{\partial x_k} + \frac{\partial u_k}{\partial x_j} + \frac{\partial u_r}{\partial x_j}\frac{\partial u_r}{\partial x_k}\right) = \frac{1+\nu}{E}\sigma_{jk} - \frac{\nu}{E}\delta_{jk}\sigma_{rr} + \delta_{jk}\alpha T \tag{12}$$

where

$\sigma_{jk} \equiv \sigma_{kj}$	are the stresses
$\epsilon_{jk} \equiv \epsilon_{kj}$	are the strains
x_k	are the cartesian coordinates
u_j	are the displacements
ρ	is the mass density
t	is time
g_j	are components of the gravity or body-force field
ν	is Poisson's ratio
E	is the modulus of elasticity
α	is the coefficient of thermal expansion
T	is the temperature above the stress-free state
δ_{jk}	is the kroneker delta, which is unity when the subscripts are equal and zero otherwise

In addition to the three dynamic equilibrium and six symmetric stress deflection relationships (Eq. 11 and 12, respectively) in nine unknowns (three deflections and six stresses), it is necessary that stresses and/or deflections be specified on the boundaries in an appropriate manner.

Length, time*, and temperature ratios are defined as before and a deflection scale, λ_u, is added to this group to give

$$\lambda_x = \frac{x'}{x}\ ,\ \tau_D = \frac{t'}{t}\ ,\quad \theta = \frac{T'}{T} \quad \text{and} \quad \lambda_u = \frac{u'}{u} \tag{13}$$

where primes again denote model parameters.

Applying Eq. 11 and 12 to the model and substituting Eq. 13, lead to the following requirements for similarity:

$$\text{(dynamic equilibrium)}\quad \frac{\sigma}{\rho} = \frac{\sigma'}{\rho'}\,\frac{\tau_D^2}{\lambda_u \lambda_x} \quad \text{and} \quad \frac{\sigma}{\rho g} = \frac{\sigma'}{\rho' g'}\,\frac{1}{\lambda_x}$$

$$\text{(stress-deflection-temperature)}\quad \frac{\lambda_u}{\lambda_x} = 1\ ,\ \frac{\nu'}{\nu} = 1\ ,\ \frac{\sigma}{E} = \frac{\sigma'}{E'}\ ,\quad \alpha = \alpha'\theta \tag{14}$$

Combining Eq. 13 and 14 yields the six dimensionless groups

$$\frac{\rho L u}{\sigma t^2},\quad \frac{\rho g L}{\sigma}\ ,\ \frac{u}{L},\ \nu\ ,\ \frac{\sigma}{E} \text{ and } \alpha T \tag{15}$$

It should be noted that the material properties, E, α, ρ and ν may be functions of temperature, T, which may itself vary with time. This thermal variation is generally much slower than the variation of deflection with time, thus justifying the distinction used between "thermal" and "dynamic" time-scales, τ_T and τ_D, respectively.

Because the analysis of aerospace structures may be simplified by considering them to be composed of bars, beams, membranes and plates, it is useful to consider the thermo-structural-dynamic equations of these elements as well. As an illustration of the derivation techniques involved, the beam element is considered in detail in the Appendix. However, the appropriate scaling parameters for several other elements are only summarized in Table 1.

2.2.2 Interpretation

The first of the preceding dimensionless groups relates to dynamic loads, the second to stresses produced by gravity effects, and the third arises in large deflection problems. The interaction among these three effects occurs when a preload

---

*In this case the time referred to is "dynamic", as opposed to the "thermal" time of Section 2.1.1.

TABLE 1 SCALING LAWS FOR ELASTIC STRUCTURAL DYNAMIC MODELS

Element	Scaled Quantity	Scaling Laws
General	Dimensions and Coordinates	$\frac{L'}{L} = \frac{x'}{x} = \lambda$
	Deflections	$\frac{u'}{u} = \frac{v'}{v} = \frac{w'}{w} = \lambda$
	Strain (linear and nonlinear)	$\frac{\epsilon'}{\epsilon} = 1$
	Time	$\frac{t'}{t} = \tau_D = \lambda \sqrt{\frac{\rho'/E'}{\rho/E}}$
	Thermal Strain	$\frac{\alpha' T'}{\alpha T} = 1$
	Frequency	$\frac{f'}{f} = \frac{1}{\lambda} \sqrt{\frac{E'/\rho'}{E/\rho}}$
Bar & Beam*	Stretching Stiffness	$\frac{(\overline{EA})'}{(\overline{EA})} = \frac{E'}{E} \lambda^2$
	Mass Per Unit of Length	$\frac{(\overline{\rho A})'}{(\overline{\rho A})} = \frac{\rho'}{\rho} \lambda^2$
	Bending Stiffness	$\frac{(\overline{EI})'}{(\overline{EI})} = \frac{E'}{E} \lambda^4$
	Twisting Stiffness	$\frac{(\overline{GJ})'}{(\overline{GJ})} = \frac{G'}{G} \lambda^4$
Membrane & Plate*	Stretching Stiffnesses	$\frac{(\overline{Eh})'}{(\overline{Eh})} = \frac{E'}{E} \lambda$
	Shearing Stiffness	$\frac{(\overline{Gh})'}{(\overline{Gh})} = \frac{G'}{G} \lambda$
	Bending and Twisting Stiffnesses $(\upsilon' = \upsilon)$ $i = x,y$	$\frac{\overline{D}_i'}{\overline{D}_i} = \frac{\overline{D}_{xy}'}{\overline{D}_{xy}} = \frac{E'}{E} \lambda^3$
	Mass Per Unit of Area	$\frac{(\overline{\rho h})'}{(\overline{\rho h})} = \frac{\rho'}{\rho} \lambda$
*Neglecting shearing deformation		

stress state, caused by gravity, influences the dynamic characteristics through a non-linear stiffness interaction. One way of seeing this directly is to consider a replica model and prototype made of the same materials. Under these assumptions Eq. 14 permits the solution:

$$\begin{aligned} \sigma &= \sigma' \\ \lambda_x &= \lambda_u = \lambda \\ \theta &= 1 \\ \tau_D &= \lambda \\ \lambda &= g/g' \end{aligned} \tag{16}$$

The significance of Eq. 16 is that the model and prototype strains and stresses are equal if the length scale equals the time scale as well as the ratio of gravitational fields between prototype and model. This latter condition on gravity field ratio is highly restrictive in selecting a model scale, but its neglect can cause significant modeling errors. Just such an effect was noted by Grimes, et al (Reference 6), who reported that joint flexibilities of a 1/10th scale model of the Saturn V were seriously affected because gravitational preload effects were not modeled properly.

Another important type of preload can occur with thermally induced stresses which are associated with the dimensionless groups αT and σ/E. As may be seen by Eq 16 (ignoring the last one on g/g'), such effects are accurately simulated in a replica model if the temperatures between model and prototype are identical.

2.3 MODELING DISTORTIONS

2.3.1 Material Considerations

Parameters associated with the use of different temperatures and materials have been investigated. Observation of the dimensionless groups associated with internal heat transmission, Eq. 6, and thermo-structural-dynamics, Eq. 15, reveals all the pertinent material properties involved in a related modeling study.

For reference purposes, Table 2 reviews the three popular orbiter design concepts, the Aluminum-Ablator or RSI/heat-sink, Titanium/TPS-protected, and Nickel-base superalloy/hot-structure, their temperature design limits, and dominant modes of internal heat transfer. The aluminum concept presents the biggest thermal modeling problems because multiple significant modes of heat transfer with conflicting scaling

laws are present. However, heat conduction in primary structure is still considered to be secondary to radiation energy transfer even for a heat-sink design. Furthermore, the aluminum concept is associated with the lowest thermal gradients and so involves the smallest thermal-dynamic interaction. For these reasons, and also because radiation effects can be modified somewhat through application of surface coatings to change emissivity, it appears that density and specific heat are the major thermal parameters to consider in selecting a model material.

TABLE 2 SHUTTLE ORBITER DESIGN CONCEPTS

Orbiter Design Concept	Primary Structure		Thermal Protection	Dominant Modes of Heat Transmission
	Material	Design Temperature		
Heat Sink	Aluminum	175°C (350°F)	Ablator or RSI	Radiation & Conduction
TPS Panels	Titanium	315°C (600°F)	Metallic & Nonmetalic	Radiation
Hot Structure	Inconel & Rene	540 (1000) & 650°C (1200°F)	None	Radiation

The key variable to consider in shuttle structural dynamic simulation is the modulus of elasticity, even though the coefficient of thermal expansion affects stiffness (through prestress level) and density influences a system's dynamic response. The reason for this is that the basic stiffness parameter, E, is temperature dependent (see Fig. 5) and temperature varies with time throughout the structure. This transient effect is accentuated in a 1/10th scale model since the time scale also shrinks to 1/10th if conduction effects are neglected. Therefore, in a transiently heated structural dynamic model it appears desirable to employ the same material and temperature levels for the model as for the prototype, particularly since the primary structure temperature levels are achievable in the laboratory (see Section 5.2); and dynamic instrumentation, which function acceptably at these thermal levels, is available (see section 5.2).

2.3.2 Geometric Considerations

The degree of geometric similarity which is maintained between any model and its prototype will influence the applicability, quantity, and type of information which may be obtained from test. Roughly speaking, the need for geometric similarity in a model is inversly proportional to the understanding of the physical phenomena involved. Thus only when the effect under investigation is fairly well understood can distorted models be useful.

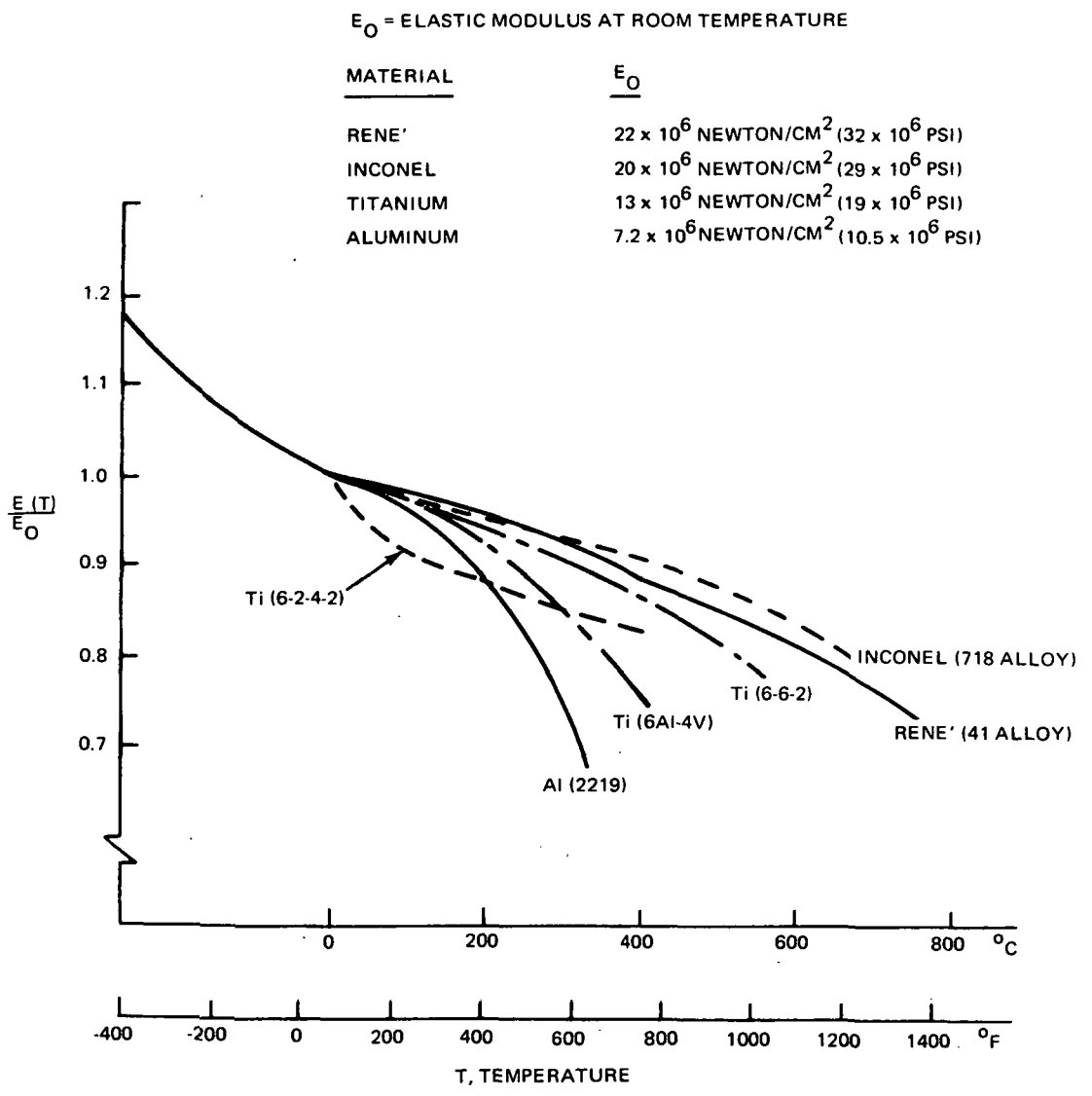

Fig. 5 Elastic Modulus Ratio, As a Function of Temperature, for Several Space Shuttle Candidate Materials

The major difficulties with replica models are associated with scaling complex joints, attachment fittings, thin skins and mechanical fasteners without seriously magnifying tolerance-error percentages. Furthermore, the costs associated with replica model manufacture, as will be shown in Section 3. 3, can become quite significant.

Therefore, the use of "adequate" models, where possible, is suggested. Illustrations of adequate modeling procedures include: replacing a corrugated spar web (acting purely as a shear panel) with a panel which matches its average shear stiffness, and substituting a stiffened cover skin with one having a different shape and number of stiffeners from the prototype, but possessing properly scaled stretching stiffnesses. However, caution must be taken to see that phenomena involving parameters which have not been scaled do not occur in either model or prototype; e. g., improper modeling in the above examples would exist if bending stiffnesses are not scaled and buckling occured in either model or prototype.

SECTION 3 MODEL DESIGN AND FABRICATION

3.1 COMPONENT DEFINITION

To better evaluate the feasibility of designing, manufacturing and testing a thermal dynamic model, as well as obtaining some idea of the cost of performing related tests, the vertical fin of an early Grumman-conceived orbiter (designated as the H3T) was selected as a focal point for detailed study. The effort described herein is a "paper study," in that an actual physical model was not built and tested. However, sufficiently realistic design and analyses have been performed and the necessary manufacturing and scaling approximations were evaluated. Thermal dynamic test and data-reduction cost estimates to conduct such a program are reported in Section 5.2.5.

Originally, the component investigated was conceptually designed as both a TPS-protected/titanium and an unprotected "hot"/inconel-rene structure. Although indications were that the fin with a TPS would be lighter, the unprotected fin was selected for detailed analysis since it posed more severe heated primary-structure design and testing problems.

To lend some perspective to the example selected, Fig. 6 presents the overall H3T orbiter. A more detailed design of the fin itself is shown in Fig. 7. Basically, the primary structure of the hot fin is comprised of a two-cell swept box beam with single-sheet/corrugated skin and truss-work ribs which attach to three fuselage ring frames at the spar roots. Figure 8 shows the detailed finite element idealization used in optimizing the fin for minimum weight and analyzing for thermal stresses.

The net airload used to design the prototype was a 9.7×10^6 newton (218,000 lb) transverse resultant, limit load. The assumed pressure distributions, which vary linerary in all directions with planform length, are shown in Fig. 9a for the tip and root section. The location of the four corners of the resulting center-of-pressure envelope are shown in Fig. 9b and, as the pressures are fully reversible, they provide eight different load conditions.

The projected surface area surrounding each note was computed and a load equal to this projected area multiplied by the average pressure at that node was calculated and placed at that node. Aerodynamic drag-loads were neglected for this phase of the analysis. As a

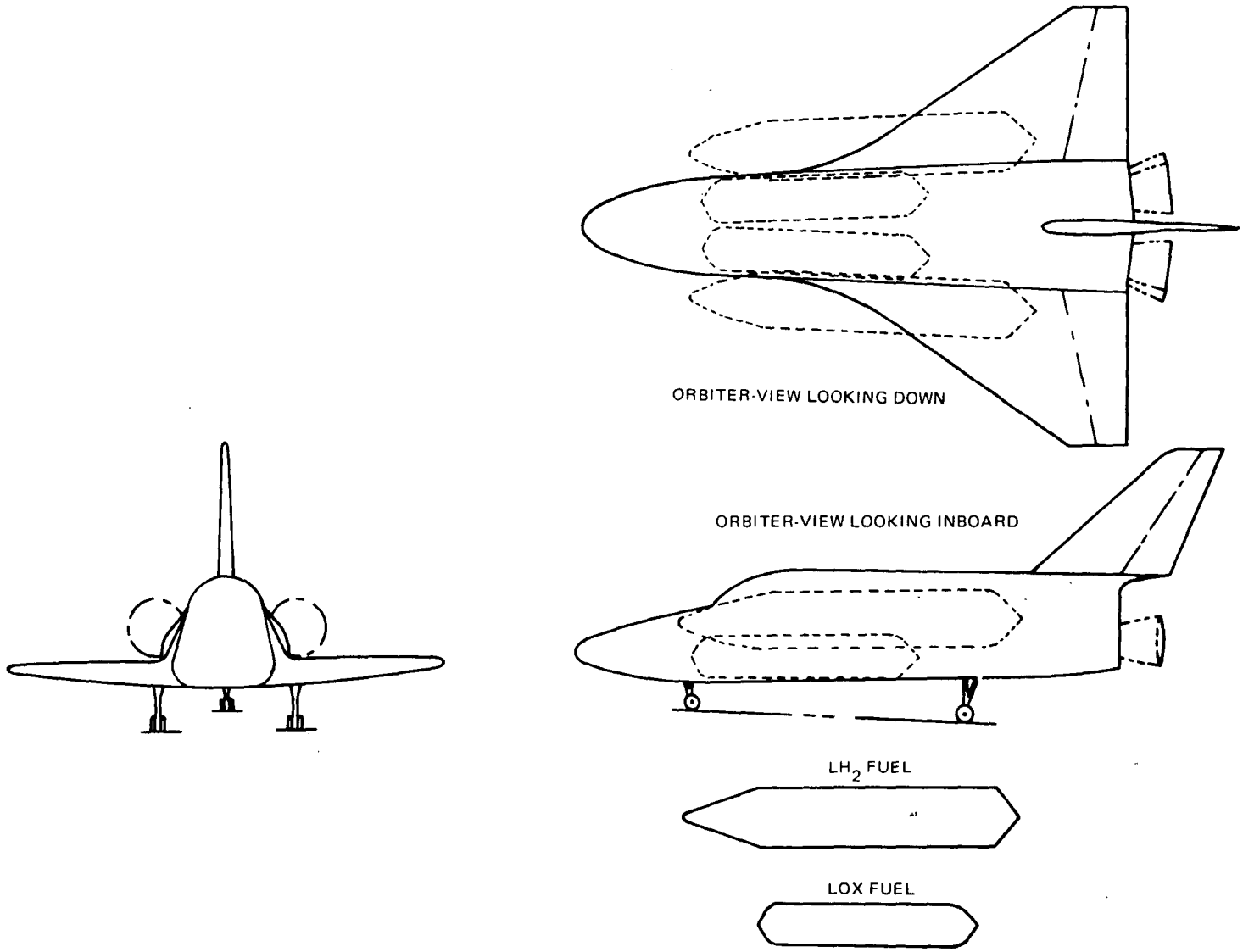

Fig. 6 Preliminary Design of Grumman H3T Orbiter

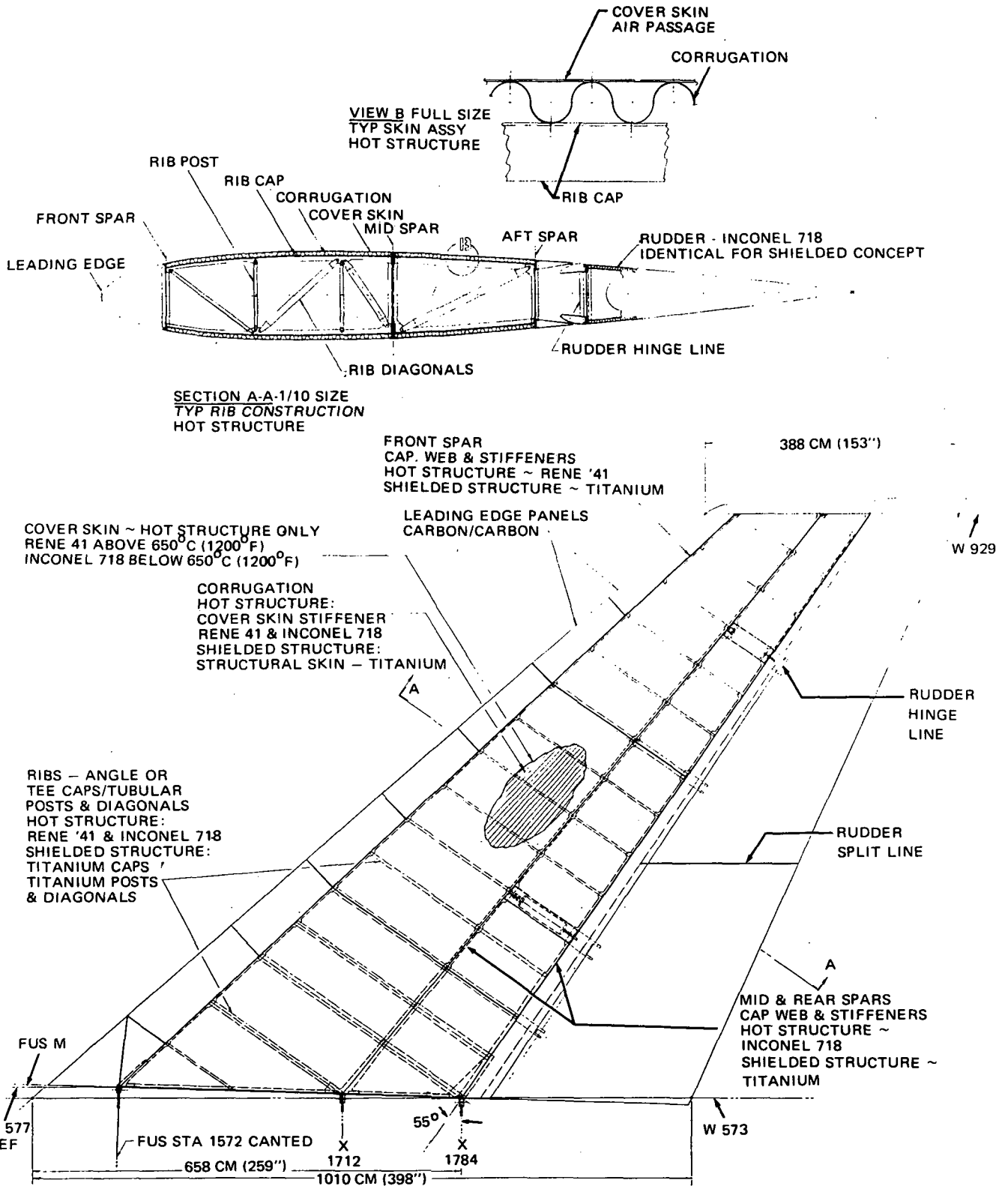

Fig. 7 Preliminary Design of H3T Orbiter Fin

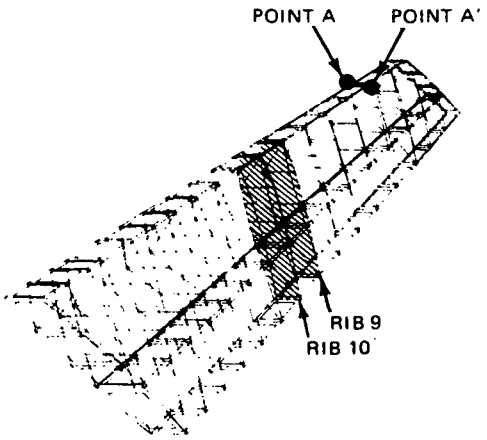

FIN WITHOUT COVERS

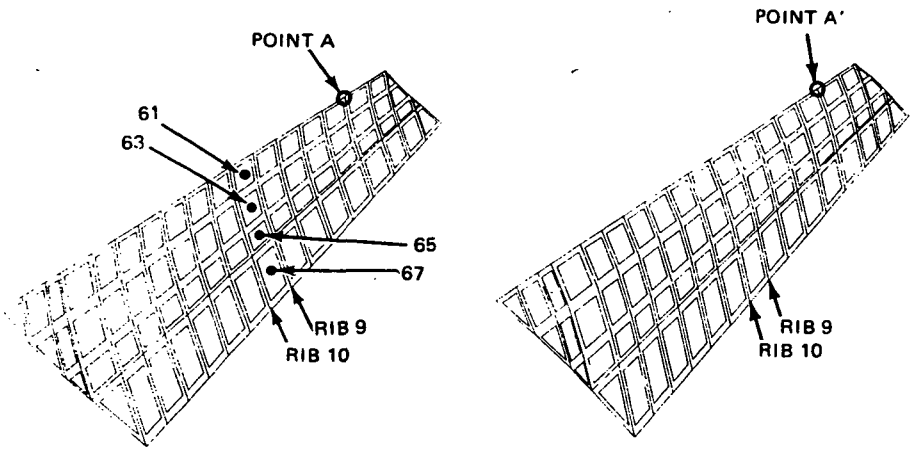

LEFT COVER

RIGHT COVER

Fig. 8 Finite-Element Idealization of H3T Orbiter Fin Structure

CONDITION	SECTION A-A	SECTION B-B
1	0.415 NEWTON/CM^2 (0.600 PSI) 75% CHORD	9.77 NEWTON/CM^2 (14.173 PSI) 75% CHORD
2	0.155 NEWTON/CM^2 (0.225 PSI) 100% CHORD	3.67 NEWTON/CM^2 (5.314 PSI)
3	8.95 NEWTON/CM^2 (12.975 PSI) 75% CHORD	3.45 NEWTON/CM^2 (4.991 PSI) 75% CHORD
4	3.36 NEWTON/CM^2 (4.865 PSI)	1.29 NEWTON/CM^2 (1.871 PSI)

a. ASSUMED CHORDWISE PRESSURE DISTRIBUTIONS

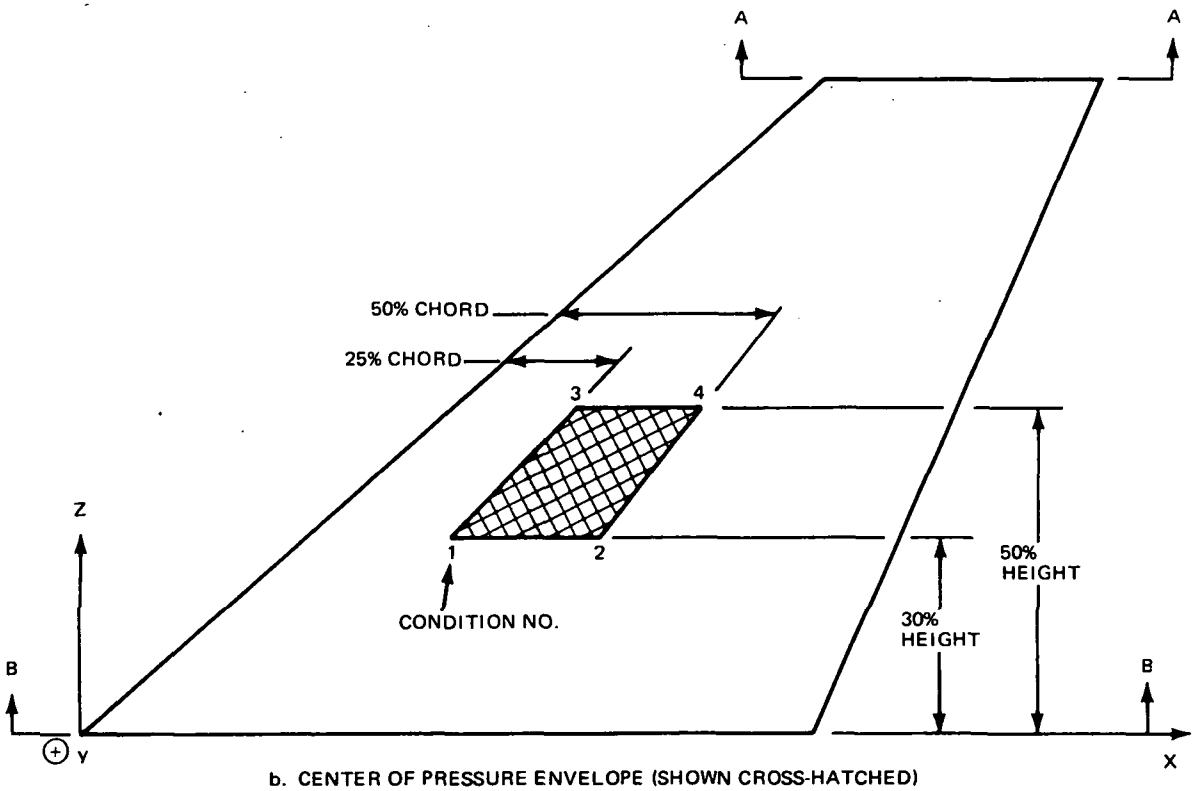

b. CENTER OF PRESSURE ENVELOPE (SHOWN CROSS-HATCHED)

Fig. 9 Design Pressures for H3T Orbiter Fin

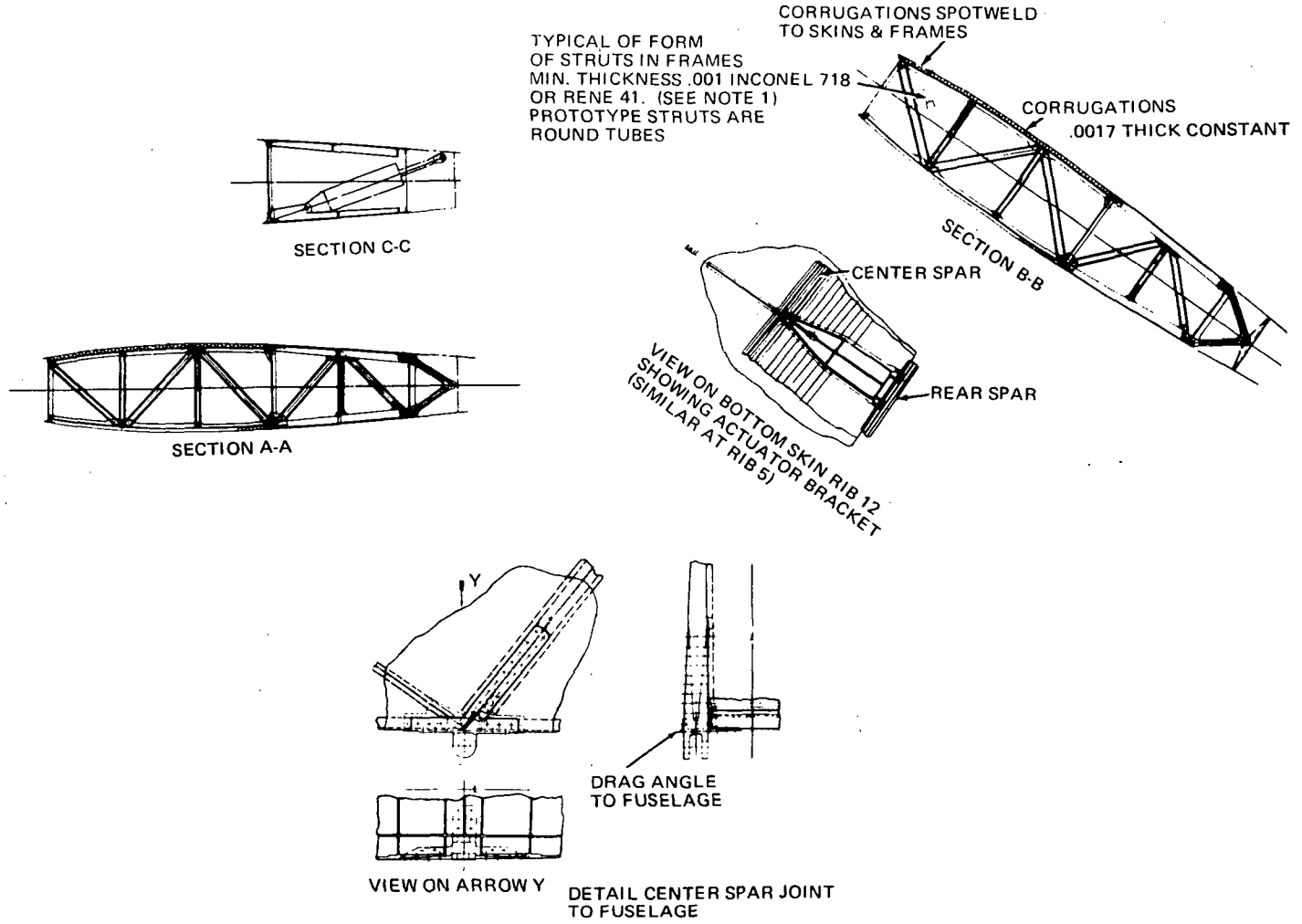

Fig. 10 1/10th Scale Thermal Dynamic Model of Shuttle Fin (Sheet 1 of 2)

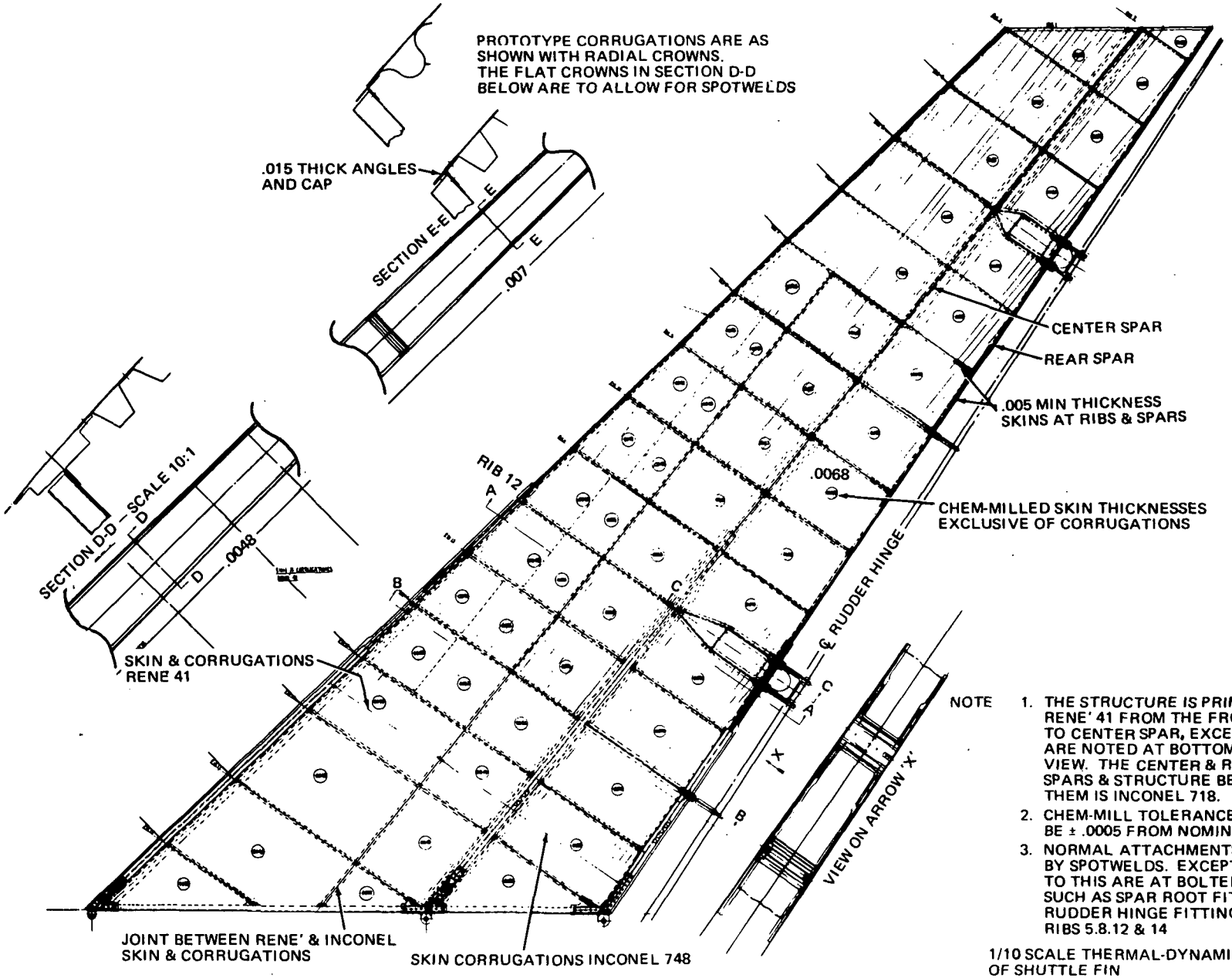

Fig. 10 1/10th Scale Thermal Dynamic Model of Shuttle Fin (Sheet 2 of 2)

precaution, the rudder was designed fail-safe, i.e., it consists of two segments, each supported by two hinges and an actuator.

The Grumman Automated Structural Optimization Computer Program (ASOP) (Reference 7) was used to automatically size the skins, webs and rib-stud members so as to minimize structural weight while not overstressing any member under the above specified airloads. Program input to ASOP involved structural idealization, material and buckling section allowables, loading conditions and practical minimum gage sizes.

3.2 MODEL DESIGN

The philosophy adopted in designing the H3T hot-fin model, similar to that used in the 1/10th scale model of the Saturn V (Reference 8), was to scale all dimensions by 1/10th and to use the same materials as the prototype where feasibility and reason permitted. The resulting design is shown in Fig. 10. Because of certain practical limitations associated with the miniaturization process, special manufacturing considerations and model distortions were necessary. The major ones are reviewed here.

- Rivets - Spot or seam welds in the model replace all rivets used in joining the corrugations to the skin face-sheet, rib, and spar-caps
- Corrugations - The shape of the skin corrugations had to be altered to provide adequate size flats to permit welding to the skin face-sheet. This caused a significant geometric distortion in the corrugated portions of the model. To validate the use of the proposed distortions, the stiffness scaling laws required that the depth, pitch, and cross-sectional area-per-pitch be closely maintained in the ratios of λ, λ, and λ^2, respectively, (where $\lambda = 1/10$ is the ratio of model length to corresponding prototype length). Figure 11 compares the prototype corrugation's cross-sectional shape with that of the model. A separate investigation was performed to estimate the skin thermal error introduced by this geometric distortion, the results of which are presented in Section 4.1.2
- Truss Members - The rib struts of the prototype are cylindrical tubes, the smallest of which have a 2.54 cm (1-in.) OD and 0.04 cm (0.016-in.) wall thickness. A 1/10th geometric scaling in such cases would be extremely costly to manufacture and a revised cross section (shown in Fig. 12) is proposed

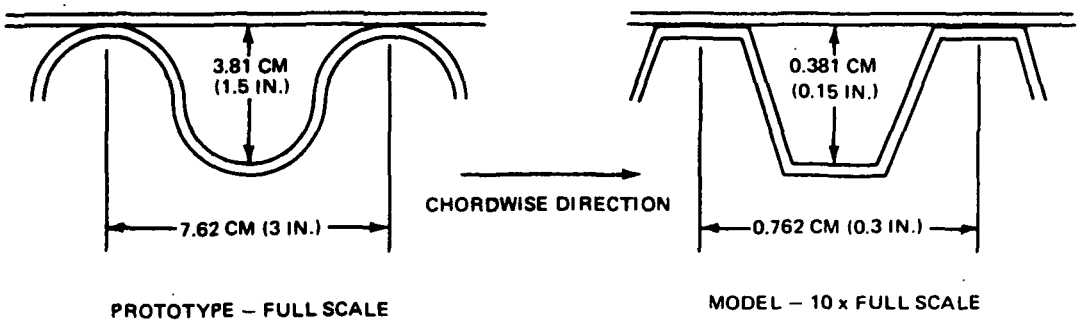

Fig. 11 Skin Design Details for H3T Orbiter Hot Fin – Prototype and Model

Fig. 12 Cross-Section for Rib Truss Braces of H3T Orbiter Hot Fin – Prototype and Model

- Skin Gages and Tolerances - In attempting to scale the variable exterior skin thicknesses, there was no point in attempting to grade them in increments of less than 0.00254 cm (0.001-in.). The reason for this is that the chem-milling process by which the sheets would be made has a ± 0.0013 cm (± 0.0005-in.) thickness tolerance. This level of gradation produces local skin stiffness distortions of the order of $\pm 15\%$. However, this figure can probably be improved upon, at additional cost, if several right and left cover-sheets are produced and the best two are selected for the model

- Scaling of Standard Size Items - Consider the difficulty associated with reducing a standard size item such as a 1 3/4 inch bolt to 1/10th size. The nearest drill to produce a hole 1/10th this size is a No. 16, which produces a 0.450 cm (0.177-in.) hole with a 0.010 cm (0.004-in.) tolerance. Therefore, either some level of compromise is required or higher costs to preserve the desired scale ratio are required

- Assembly - Once the spar and rib members have been manufactured, the entire substructure, with the exception of the root and tip ribs, are positioned in a jig and spot welded together. Only one side of the skin corrugation is then welded in place. This is followed by welding the corresponding facesheet using copper bars which slide in the spanwise direction through the corrugation crests, thereby providing back-up supports and electrical conductors for the welding operation. The second side of the fin is next assembled in the same order and manner. The assembly is completed by welding the root and tip ribs in place. Although machining of the spars, root joints, rudder actuator, and hinge pick-up fittings of the model appears feasible, many distortions from the prototype are expected, particularly those of the types presented in Figures 45-49 of Reference 8 in which small machining details were omitted or simplified

3.3 MODEL MANUFACTURING COSTS

For a program involving a reduced scale replica model, manufacturing represents the major expense of the overall program. The reason for this is that the necessary miniaturization of members and gages requires elaborate handling procedures and attachment techniques requiring the development of special tooling fixtures, equipment handling, and fabrication methods. Table 3 summarizes the estimated

TABLE 3 MAN-MONTHS ESTIMATE FOR FABRICATION OF 1/10th SCALE HOT FIN REPLICA MODEL

Responsibility / Task	Engineering	Production Shop	Tool Methods Design	Tool & Jig Fabrication	Mfg. Mgmt & Control	Quality Control	Total
Welding Methods Support	6 1/2	-	-	-	-	-	6 1/2
Fabrication	-	22	3	8	-	-	33
Assembly	-	40	2	8 1/2	-	-	50 1/2
Tooling	-	-	1 1/2	1	-	-	2 1/2
Special Equipment and Handling	-	-	6	2 1/2	4	-	12 1/2
Inspection	-	-	-	-	-	6	6
TOTAL	6 1/2	62	12 1/2	20	4	6	111

participation levels, by function, required for manufacturing the fin model. The material cost for the necessary amounts of rene 41 and inconel 718 are estimated at $6500, while the outside-vendor costs for chem-milling the variable-gage flat skins have been approximated at $50,000 for two complete sets. It should be noted that all labor time estimates have approximately a ±20% tolerance associated with them. Furthermore, it is estimated that an additional 5 man-months of engineering design and stress analysis would be required, beyond the level demonstrated by Fig. 10, to produce a complete set of drawings for the 1/10th scale fin model.

SECTION 4 THERMO-STRUCTURAL ANALYSES AND MODELING ERRORS

4.1 THERMAL ANALYSES

4.1.1 Lumped Analysis of Entire Fin Structure

The section of fin analyzed is bounded by the carbon/carbon leading edge, the aft-fuselage, and the rudder. These three interfaces are considered to be adiabatic surfaces in the thermal idealization.

The fin thermal nodes were divided into cover, web, diagonal and stud-member nodes, as well as corner nodes, thus making them correspond almost identically to the structural model members and nodes (Fig. 8). The node locations for a typical chordwise segment are shown in Fig. 13. Prior to earth touchdown, a "space sink" at -273°C (-460°F) was represented by a fictitious node. After touchdown, the external surfaces of the fin were convectively coupled to ambient air at 20°C (70°F) through a second fictitious node.

Thermal properties and heat transfer coefficients used in calculating thermal capacitance, and conductive, convective, and radiative couplings are listed in Table 4.

TABLE 4 THERMAL PROPERTIES AND COUPLINGS FOR THE HOT FIN NETWORK

Material	Thermal Capacity, c_p $\frac{\text{g-cal}}{\text{gm-}^\circ\text{C}}$ (Btu/lb-°F)	Density, $\frac{\text{gm}}{\text{cm}^3}$ (lb/in.^{3})	Thermal Conductivity, k $\frac{\text{g-cal}}{\text{m-sec-}^\circ\text{C}}$ (Btu/sec-in.-°F)
Rene	0.12 (0.12)	8.23 (0.297)	3.45(1.93 x 10^{-4})
Inconel	0.12 (0.12)	8.23 (0.297)	3.45(1.93 x 10^{-4})
Heat transfer coefficient between Fin/Ambient Air, h= 0.367 $\frac{\text{g-cal}}{\text{Hr-cm}^2\text{-}^\circ\text{C}}$			
Panel emissivity, $\varepsilon = 0.8$			(.75 Btu/Hr-ft^2-°F)

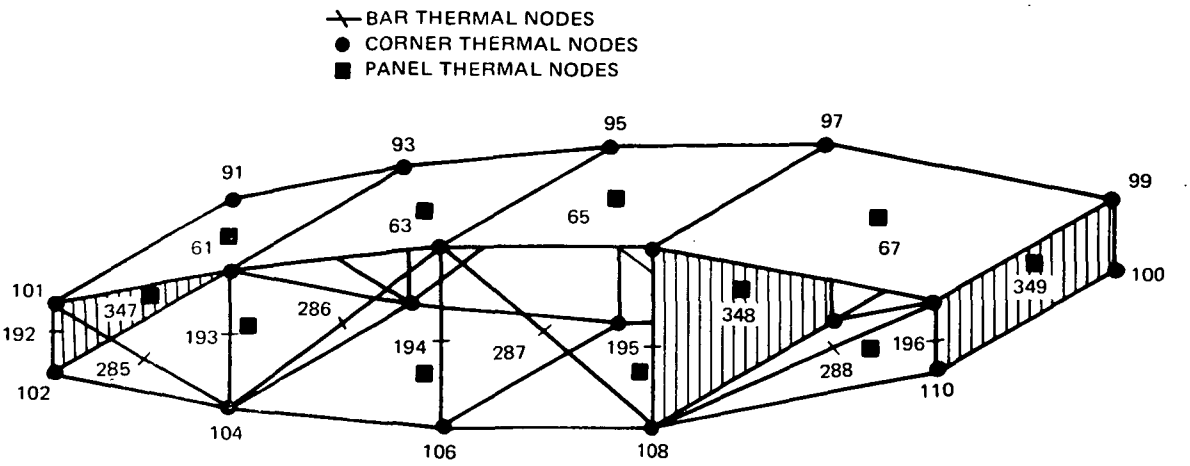

Note: For clarity, some nodes have been left unnumbered in the sketch

Fig. 13 Thermal Structural Idealization of H3T Orbiter Fin Between Ribs 9 and 10

Preliminary analyses of the H3T configuration had shown that maximum temperature gradients would occur in the fin during reentry. Therefore, this condition was analyzed in detail. Reentry heat flux as a function of time for a 650°C (1200°F) isotherm is shown in Fig. 14. Heat flux levels at other locations of the fin were estimated using a fourth-power-law ratio. For example, the heat flux at the 540°C (1000°F)* isotherm, $\dot{q}_{1000}$, was determined by using the relation:

$$\dot{q}_{1000} = \dot{q}_{1200} \left(\frac{T_{1000}}{T_{1200}} \right)^4$$

where

$$T_{1000} = 810^{\circ}K \ (1460^{\circ}R) \qquad T_{1200} = 920^{\circ}K \ (1660^{\circ}R)$$

Using an initial uniform temperature of 71°C (160°F) and reentry heat flux boundary conditions and the thermal network described, thermal analyses were performed for both prototype and 1/10th scale model. Detailed digital results for each 60-second time interval for the prototype and 6-second interval for the model were obtained, and temperature history plots were made for each prototype structural element between ribs 9 and 10 (see Fig. 8). Once the required scale shift factor of 10 is made in prototype to model time, the prototype and model plots were found to overlap for the scale used in Fig. 16, 17, 18, and 19. The results for panels 61, 63, 65 and 67 are presented in Table 5 and the associated scaling temperature errors are plotted in Fig. 20.

Since these results are typical of other panels throughout the idealized fin, a more careful search of the digital printout was made to determine the greatest error in nodal temperature throughout the structure. Points A and A' of Fig. 8, which are located at the intersection of a rib and the front spar, indicated the greatest discrepancies. Temperature history plots for these points in the model and prototype are compared in Fig. 21. The results may be interpreted as follows: since only radiation was scaled accurately, the largest scaling errors occur during periods of maximum conduction to interval radiation flux ratios. Because this ratio is approximately inversely proportional to absolute temperature level to the third power, thermal modeling errors are lowest at times corresponding to the higher temperature levels (e.g between 40 and 180 seconds of model time in Fig. 21). Another

---

*See Fig. 15 for the 540°C (1000°F) isotherm location.

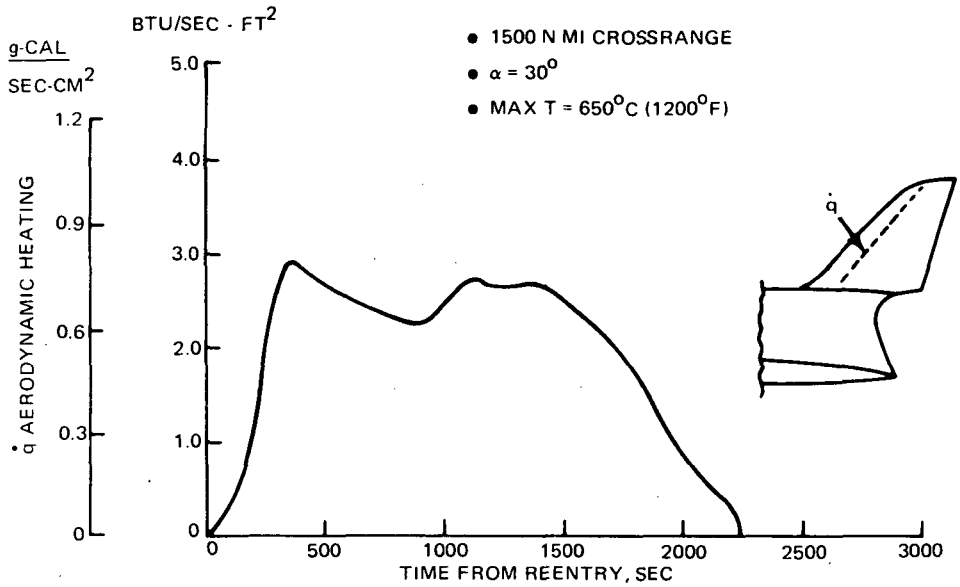

Fig. 14 H3T Vertical Fin Reentry Heat Flux for 650°C (1200°F) Isotherm

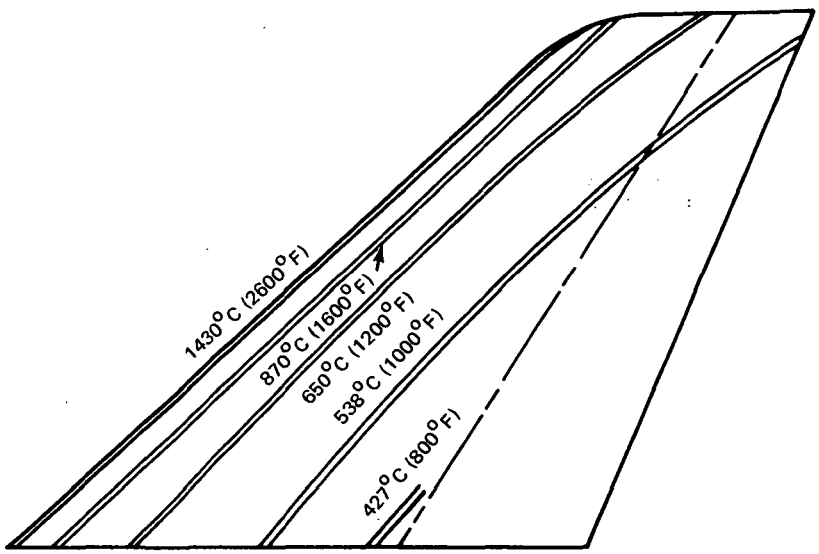

Fig 15 Maximum Fin Isotherms

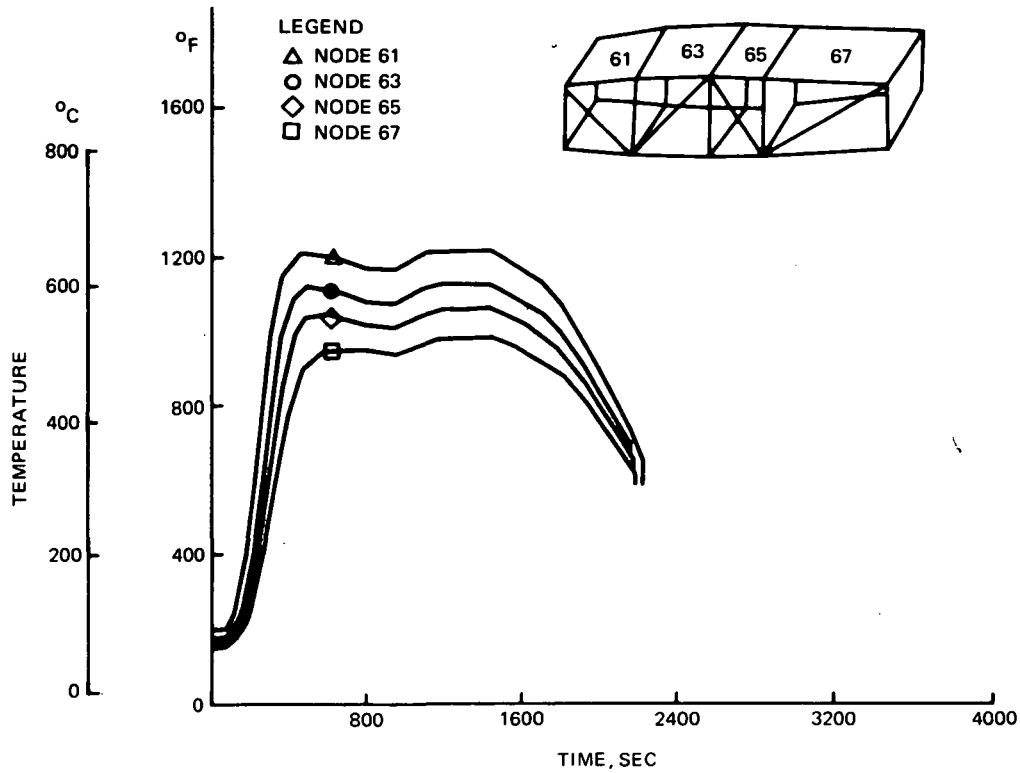

Fig. 16 H3T Fin Thermal Analysis – Cover Nodes 61, 63, 65 and 67

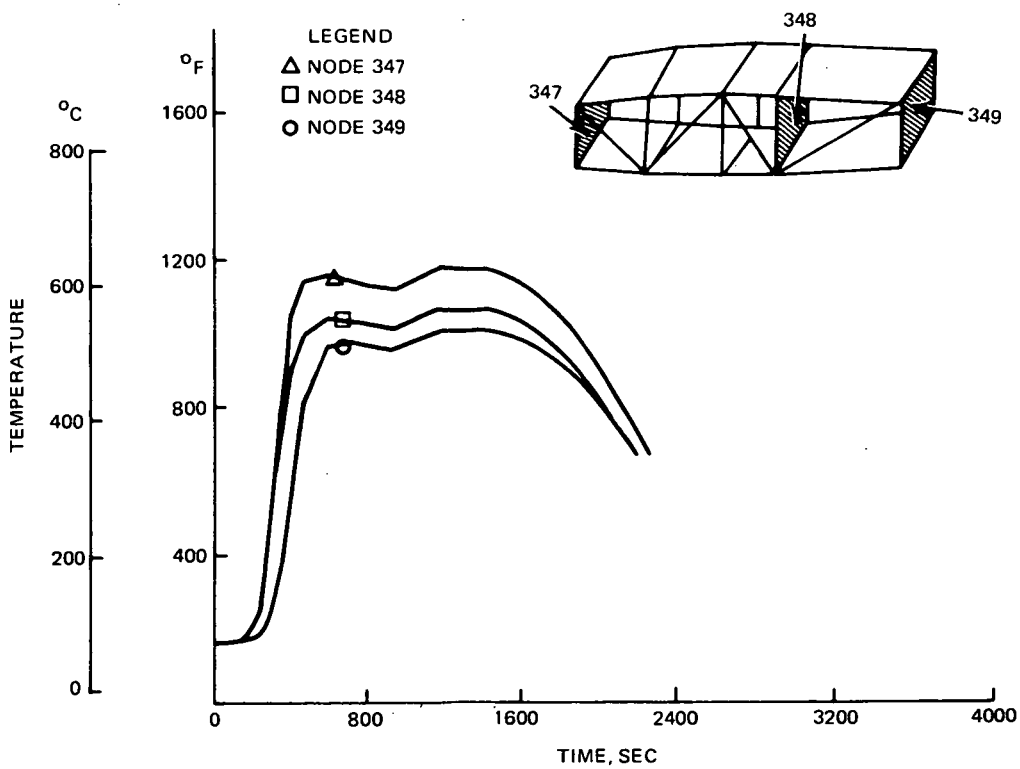

Fig. 17 H3T Fin Thermal Analysis – Spar Nodes 347, 348, 349

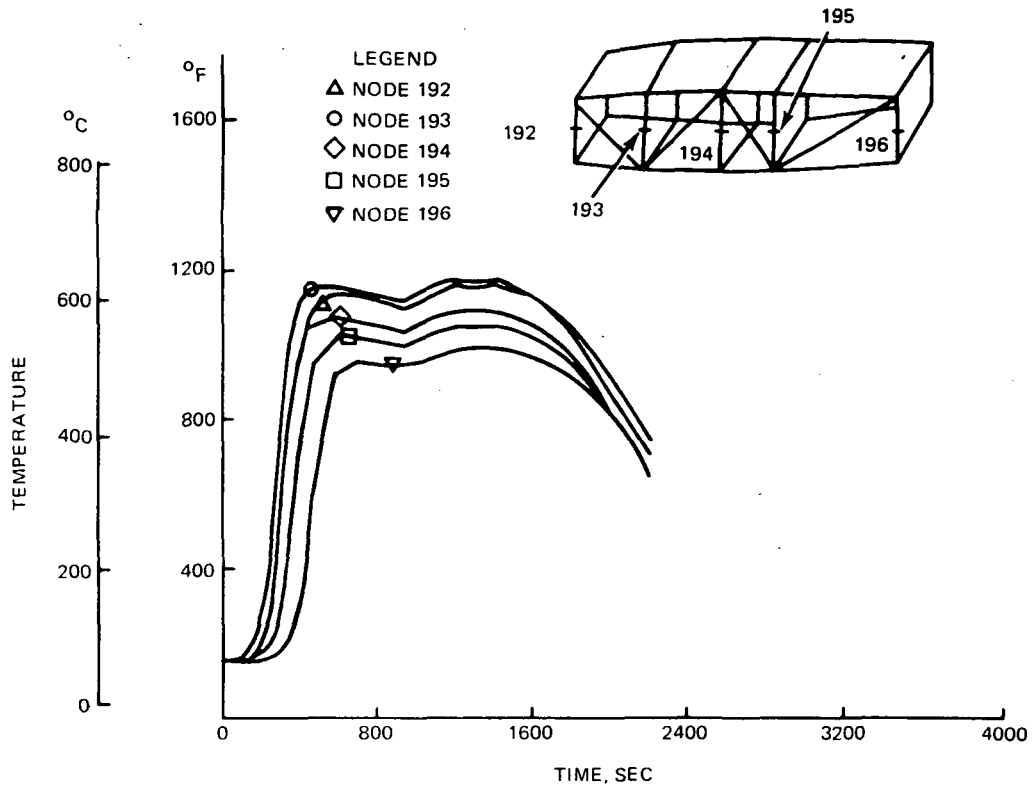

Fig. 18 H3T Fin Thermal Analysis – Vertical Truss Nodes 192 Through 196

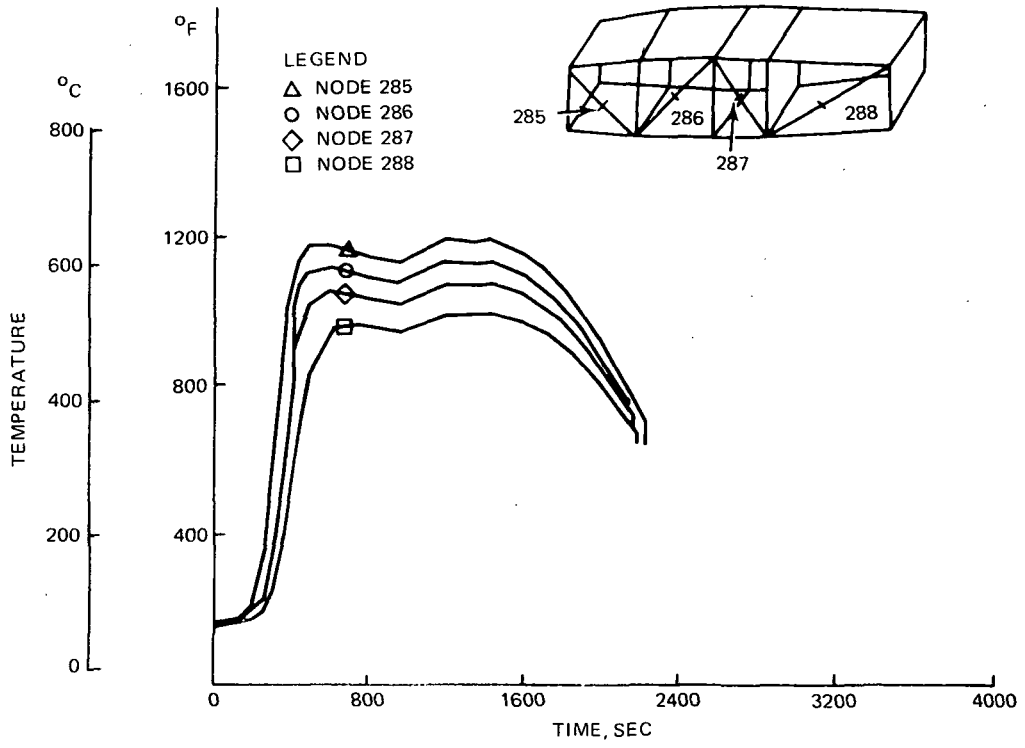

Fig. 19 H3T Fin Thermal Analysis – Diagonal Truss Nodes 285 through 288

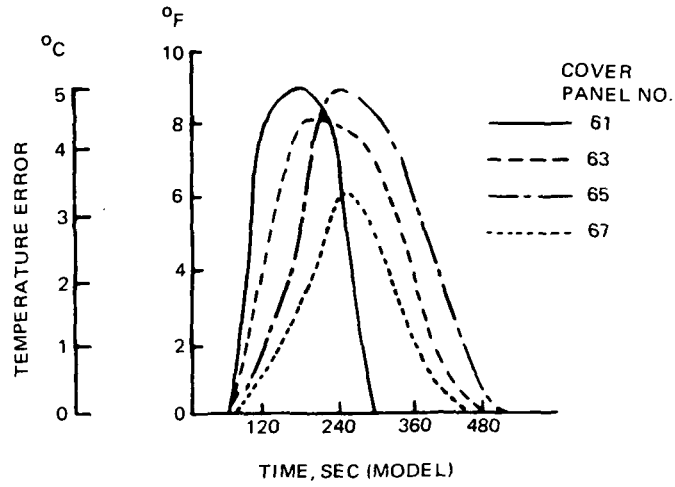

Fig. 20 Cover Panel Temperature Errors in Hot Fin Model

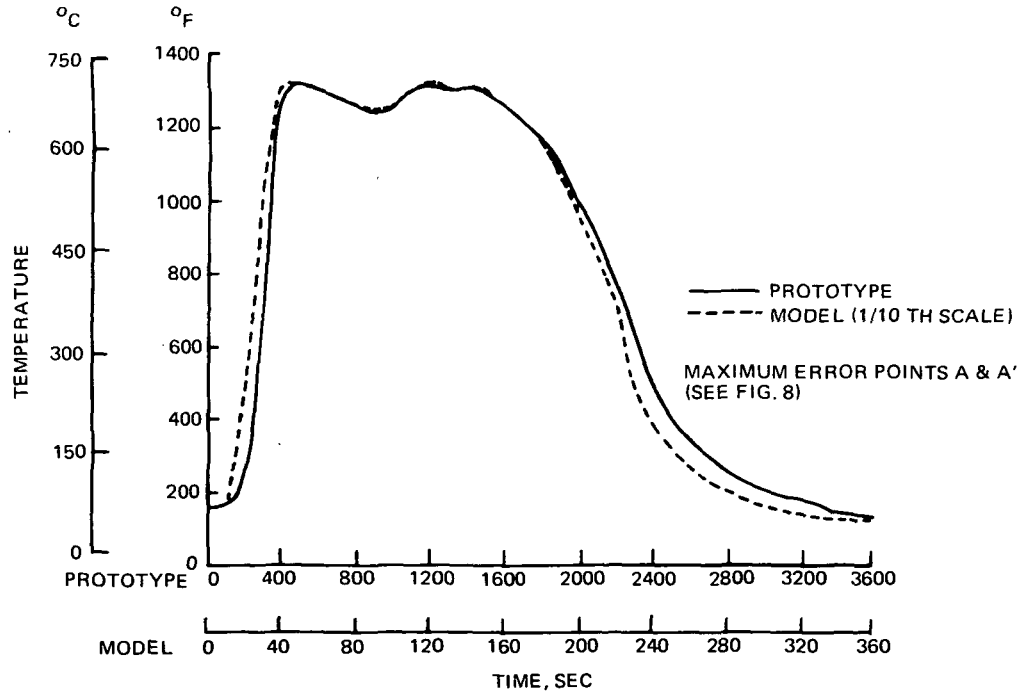

Fig. 21 H3T Hot Fin Thermal Analysis – Maximum Error Points A and A'

TABLE 5

COVER SKIN TEMPERATURES - °C (°F) - IN PROTOTYPE AND MODEL OF H3T ORBITER FIN

Member No.		61		63		65		67	
Time after reentry (sec)		Prot.	Model	Prot.	Model	Prot.	Model	Prot.	Model
Prototype	Model								
0	0	71(160)	71(160)	71(160)	71(160)	71(160)	71(160)	71(160)	71(160)
60	6	72(161)	72(161)	71(160)	71(160)	71(160)	71(160)	71(160)	71(160)
120	12	114(238)	119(246)	93(200)	95(204)	84(183)	85(185)	80(176)	81(178)
180	18	214(417)	219(426)	154(309)	158(317)	125(257)	128(262)	113(236)	115(239)
240	24	356(679)	360(686)	258(496)	265(508)	199(390)	204(399)	172(342)	176(348)
300	30	525(977)	525(977)	415(778)	419(785)	324(616)	329(624)	270(519)	273(523)
360	36	620(1147)	620(1147)	538(1000)	540(1003)	452(845)	455(851)	374(704)	377(707)
420	42	649(1200)	650(1202)	588(1091)	590(1093)	527(981)	530(984)	445(832)	446(835)
480*	48*	658(1214)	658(1214)	603(1116)	603(1116)	557(1033)	557(1033)	485(903)	485(903)

* Temperature results for these members after 480 prototype and 48-model seconds are essentially identical.

significant fact is that the largest errors occur at nodes with the largest conduction couplings. Since the analysis is based upon a discrete idealization of properties which are actually distributed, it is felt that the above errors are conservative and represent upper limits to those anticipated in an actual hardware test.

4.1.2 Detailed Analysis of Corrugated Covers

Three main sources of temperature-error exist in the model's corrugated covers. These are due to the (1) difference in model time-scale between radiation and conduction heat transfer of a reduced scale model, (2) distortions required by the weld-flats in the model, and (3) gage-size tolerances which have a much greater effect upon the model than the prototype.

The effect of each of these was evaluated by conducting simulated reentry analyses for separate thermal idealizations (see Fig. 22) of a typical segment. Analysis of the following four thermal idealizations were performed:

- Prototype covers
- 1/10th size perfect replica model of covers
- 1/10th size distorted model (corrugations flattened at crest and trough)
- 1/10th size distorted model with maximum material gage size error tolerance

Results of the four analyses are presented in Table 6 and Fig. 23 through 25. They indicate that the temperature errors are slight, major errors are associated with earlier reentry times, and that they are attributable to the inevitable conduction/radiation model time-scale discrepancy.

4.2 STRUCTURAL ANALYSES

4.2.1 Lumped Analysis of Entire Fin Structure

Since the maximum temperature errors between replica model and prototype are of the order of 5%, application of the scaling laws indicates that thermal strains and stresses will be almost identical. Hence, they were only calculated for the prototype.

Preliminary evaluation of the maximum temperature gradient between ribs 9 and 10 from the curves of Fig. 16 through 19 indicated that it occurred within 600

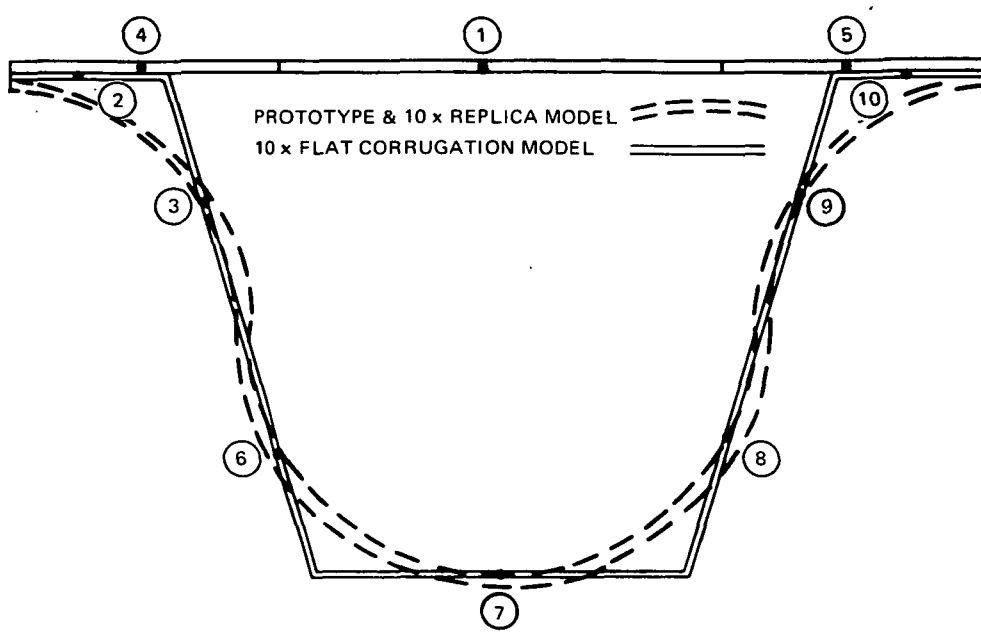

Fig. 22 Hot Fin Cover Thermal Idealizations

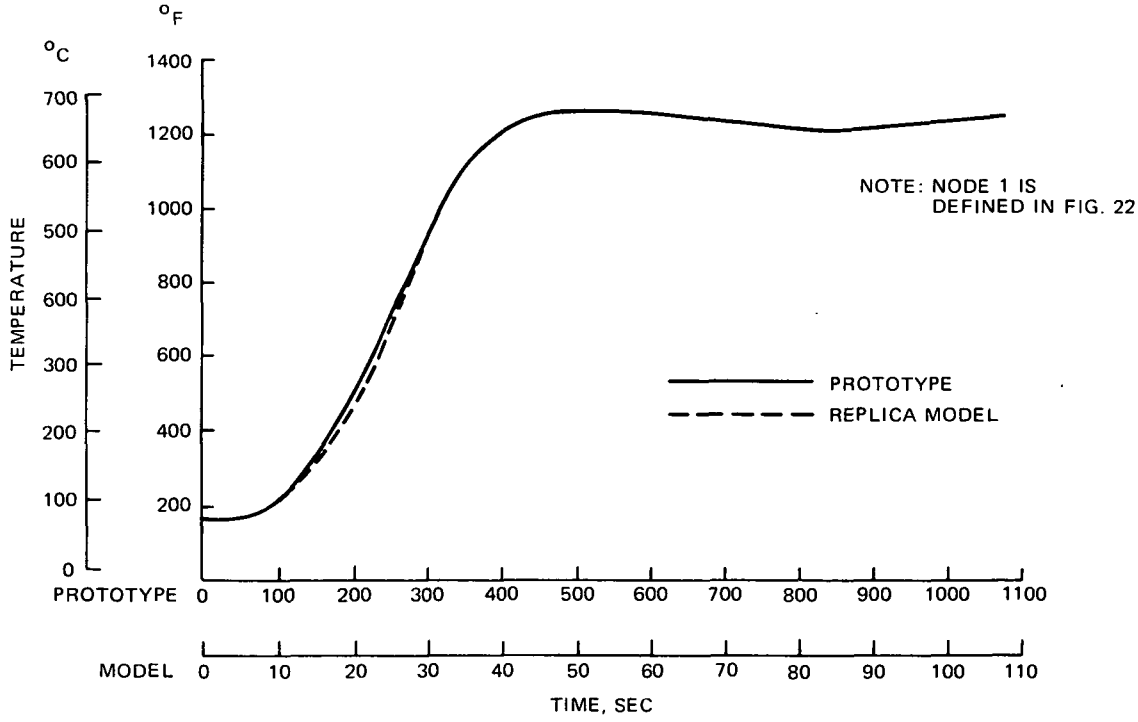

Fig. 23 Hot Fin Cover Thermal Analysis – Node 1

TABLE 6 COMPARATIVE TEMPERATURE (^{o}C(^{o}F)) RESULTS OF COVER SKIN THERMAL ANALYSIS FOR HOT FIN REENTRY

Prot Time (Sec)	NODE 1* Prototype	NODE 1* Model Replica	NODE 1* Model Flat Corrug.	Model Flat Corrug. Minus 0.00127 cm (0.000 5 in)**	NODE 7* Prototype	NODE 7* Model Replica	NODE 7* Flat Corrug.	Model Flat Corrug. Minus 0.00127 cm (0.000 5 in)**
0.	71(160)	71(160)	71(160)	71(160)	71(160)	71(160)	71(160)	71(160)
60	74(166)	74(165)	74(166)	74(166)	71(160)	71(159)	71(159)	71(159)
120	125(258)	121(249)	120(248)	121(249)	79(174)	88(191)	87(189)	87(189)
180	222(431)	208(406)	207(404)	208(407)	120(249)	152(305)	147(296)	148(299)
240	352(665)	336(637)	335(635)	338(641)	226(438)	265(510)	254(490)	258(497)
300	504(938)	495(923)	494(921)	499(929)	414(777)	442(827)	425(796)	430(807)
360	615(1139)	614(1137)	613(1134)	615(1141)	575(1068)	575(1068)	575(1068)	580(1078)
420	665(1227)	666(1229)	665(1226)	666(1230)	653(1206)	658(1215)	652(1205)	655(1211)
480***	680(1254)	680(1254)	679(1253)	680(1255)	675(1248)	677(1251)	675(1248)	676(1250)
	NODE 3*				NODE 4*			
0	71(160)	71(160)	71(160)	71(160)	71(160)	71(160)	71(160)	71(160)
60	71(160)	72(161)	72(161)	72(162)	74(165)	74(165)	74(165)	74(165)
120	90(184)	98(209)	100(213)	101(214)	118(245)	116(240)	114(238)	116(240)
180	137(278)	170(338)	173(343)	174(346)	204(399)	199(390)	197(387)	199(391)
240	242(469)	286(547)	289(552)	293(559)	326(618)	324(615)	323(613)	327(620)
300	478(791)	455(851)	455(850)	460(859)	480(894)	485(904)	485(904)	490(913)
360	578(1072)	594(1101)	590(1095)	596(1104)	602(1115)	609(1127)	608(1126)	612(1133)
420	653(1207)	659(1218)	658(1214)	660(1219)	659(1219)	664(1225)	663(1224)	665(1228)
480***	675(1249)	677(1252)	676(1250)	677(1252)	678(1251)	679(1253)	679(1253)	680(1255)

*See Fig. 22 for identification of node number
**Maximum gage size error.
***All results after 480 sec are identical for each model

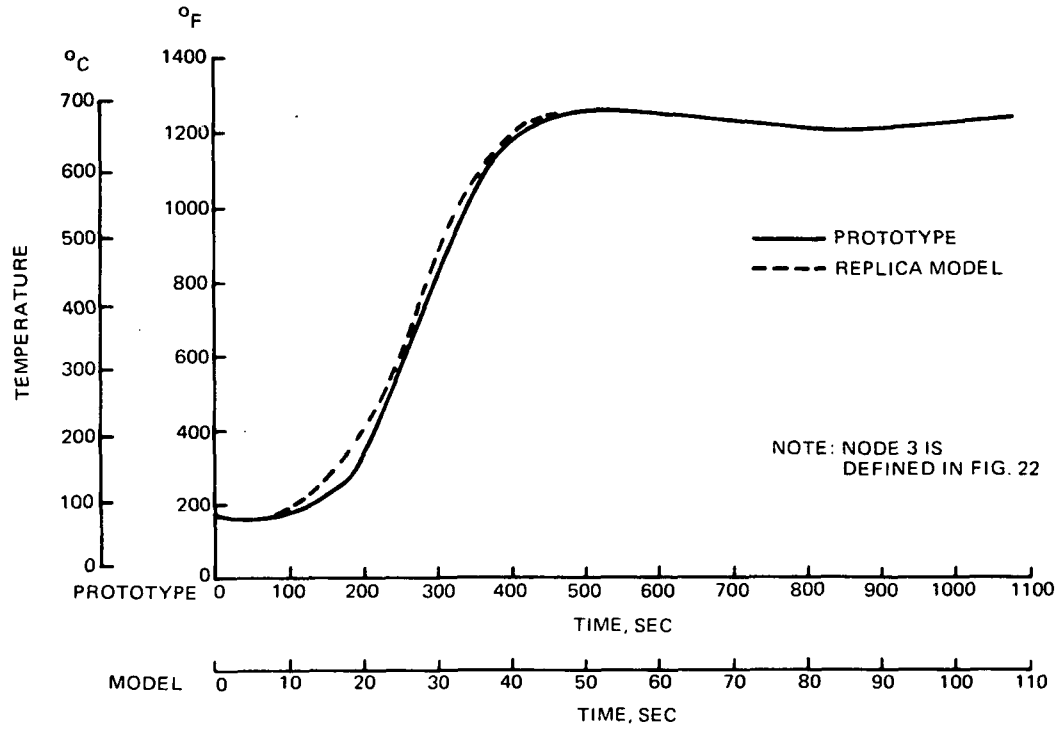

Fig. 24 Hot Fin Cover Thermal Analysis – Node 3

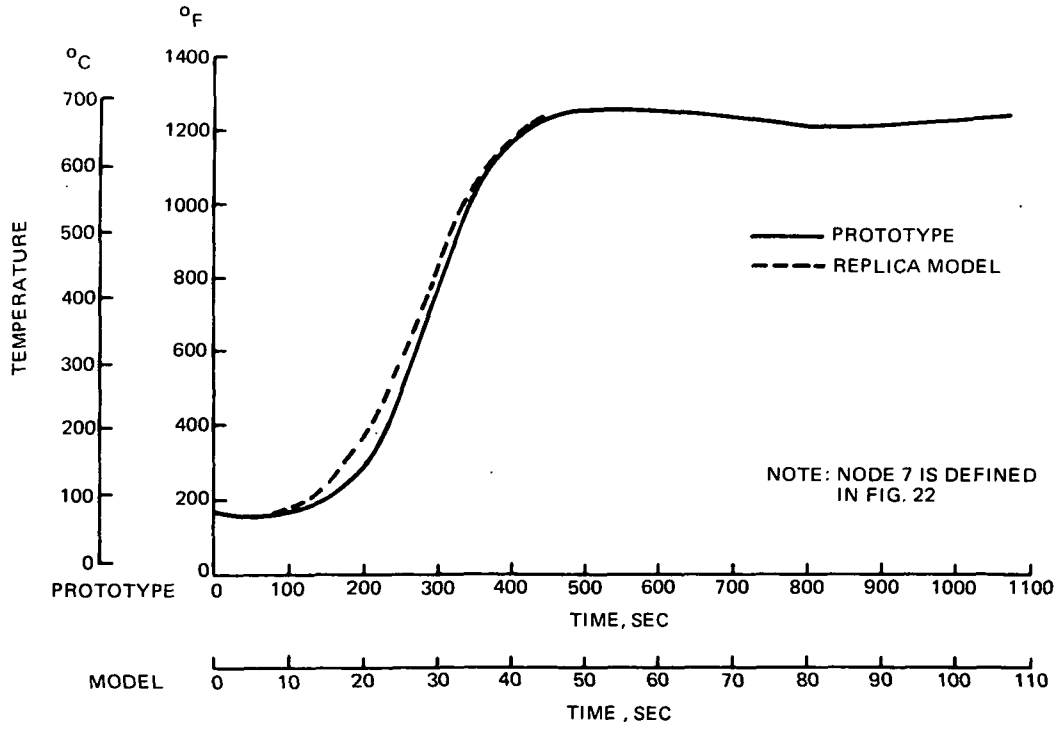

Fig. 25 Hot Fin Cover Thermal Analysis – Node 7

seconds after reentry. A more precise evaluation of the maximum gradient condition, using computer printout, revealed that the maximum chordwise gradient occurred at approximately 300 and 420 seconds after reentry. Therefore, finite element internal thermal load analyses were performed for the 300- and 420-second time-slice temperature distributions. Because of necessary assumptions associated with the finite element method the covers, which consist of outer flat sheets attached to corrugated inner sheets, were idealized as single orthotropic membrane elements. The results showed no significant differences in internal load intensities between 300 and 420 seconds. Furthermore, these loads were an order of magnitude lower than those caused by the peak mechanical air loads used for design purposes. Similar to the mechanical loading cases, the thermally induced primary stresses in the orbiter fin were in the spanwise direction, although secondary loads also occurred in the chordwise and thickness directions. Inasmuch as the material allowables at peak reentry temperatures are only reduced by approximately 20%, the thermal stresses do not appear critical in themselves.

Fig. 26 shows the thermally induced average spanwise coverloads between ribs 9 and 10 computed by the finite element program and classical beam theory. As may be seen, the loads determined by beam theory are quite accurate and slightly conservative. This is to be expected as a key assumption of beam theory is that sections normal to the spanwise axis remain plane while heated. Since this assumption introduces more severe constraints than actually exists, the more accurate finite-element results are slightly lower and permit the calculation of thickness and chordwise stresses. However, the relative simplicity and accuracy associated with the use of elementary beam theory for the entire cross section justified its use for obtaining the stress results which follow.

A comparison of spanwise loads in corrugated and noncorrugated spar web designs for the 300 second time slice are presented in Table 7. The results clearly demonstrate how the corrugations greatly releave the loads induced in the forward (hotter) external skins as well as in the spar webs themselves.

4.2.2 Detailed Analysis of Corrugated Skin

A more detailed thermal analysis of the cover (see Fig. 22) between ribs 9 and 10, which permitted the determination of temperature differences in the built-up construction, revealed that the 300-second time slice produced more severe cover

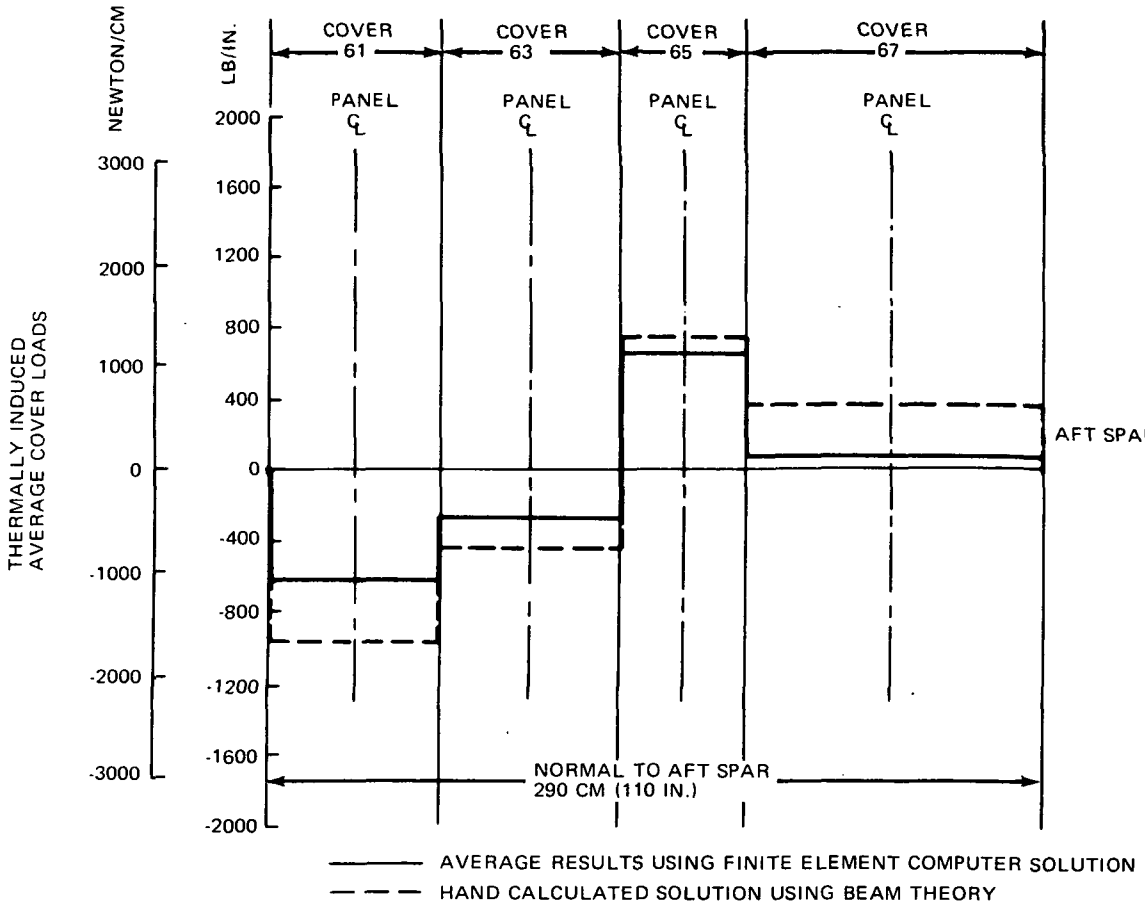

Fig. 26 Average Spanwise Cover Loads at 300 Seconds After Reentry

TABLE 7 AVERAGE STRESSES IN CORRUGATED AND NON CORRUGATED H3T HOT FIN SPAR-WEB 300-SECOND TIME SLICE

Element	Number (See Fig. 13)	Case**	Average Stress*	
			newtons/cm^2	(psi)
Front Spar Web	347	C	0	(0)
		N	65,700	(95,250)
Front Spar Cap	623	C	51,100	(74,100)
		N	40,700	(59,000)
Front Cover	61	C	-13,100	(-19,000)
		N	-22,100	(-32,000)
Second Cover	63	C	-4,490	(-6,500)
		N	-11,000	(-16,000)
Third Cover	65	C	6,900	(10,000)
		N	1,380	(2,000)
Mid-Spar Web	348	C	0	(0)
		N	24,500	(35,500)
Mid-Spar Cap	629	C	26,900	(39,000)
		N	22,000	(32,000)
Aft Cover	67	C	3,450	(5,000)
		N	0	(0)
Aft Spar Web	39	C	0	(0)
		N	32,600	(47,300)
Aft Spar Cap	631	C	26,400	(38,250)
		N	24,400	(35,400)

*Does not include stress resulting from temperature variation through the thickness of the cover skin. These latter self-equilabrating stresses must be superimposed upon the above cover stresses.

**C = corrugated

**N = noncorrugated

stress than the 420 second time slice. Thus, thermal stresses in the covers between ribs 9 and 10 are presented only for the 300-second time condition (see Table 8).

4.2.3 Effect of Heating Upon Bending and Twisting Stiffness

Since the fin is free to expand in the spanwise direction, the effect of temperature upon the bending stiffness is primarily due to a reduction in material allowables which, for the materials and temperatures considered, is under 20%.

An equation relating the change in torsional stiffness of a beam-type structure during heating, which causes a reduction in material properties and axial stresses, is (see References 9 and 10):

$$\frac{(\overline{GJ})_{eff}}{(\overline{GJ})_o} = \frac{(\overline{GJ})_H}{(\overline{GJ})_o} + \frac{\int_A \sigma_x \, r^2 \, dA}{(\overline{GJ})_o}$$

where $\overline{GJ}$ are twisting stiffnesses of the cross-sections, the σ_x are spanwise stresses, and the subscripts "o" and H correspond to unheated and heated conditions, respectively.

The twisting stiffnesses were computed by modifying the thin walled multi-cell torsion formula given in Reference 11 to include a variable shear modulus, G, which depends upon temperature. Results for the corrugated shear web design are:

$$(\overline{GJ})_o = 117 \times 10^3 \text{ newtons - m}^4 \; (63.2 \times 10^9 \text{ lb-in.}^4)$$

$$\frac{(\overline{GJ})_H}{(\overline{GJ})_o} \times 100 = 92.5\%$$

$$\frac{\int_A \sigma_x \, r^2 \, dA}{\overline{GJ}_o} \times 100 = -.25\%$$

$$\frac{(\overline{GJ})_{eff}}{(\overline{GJ})_o} \times 100 = 92.2\%$$

It should be observed that the effect of spanwise stress upon torsional compliance is extremely small in this case while the reduction in material properties causes the primary change in twisting stiffness.

TABLE 8 H3T FIN MID-PANEL SKIN STRESSES BETWEEN RIBS 9 AND 10
(REF. FIG. 8) AT 300 SECONDS AFTER REENTRY

Stress - newton/cm^2 (psi) See sketch below for points at which stress is given							
Panel No.	Material	1	2	3	4	5	6
61	Rene	-12,300(-17,850)	-5,450(-7,900)	-5,170(-7,500)	11,300(16,400)	14,200(21,300)	13,700(19,900)
63	Inconel	-13,400(-19,400)	1,031 (1,500)	1,310 (1,900)	14,900(21,600)	20,100(29,200)	19,900(28,800)
65	Inconel	-3,590 (-5,200)	3,170 (4,600)	3,450 (5,000)	26,400(38,300)	32,500(47,100)	32,500(47,100)
67	Inconel	-11,900(-17,200)	-12,800(-18,500)	-5,520(-8,000)	14,300(21,400)	20,200(29,250)	20,200(29,250)

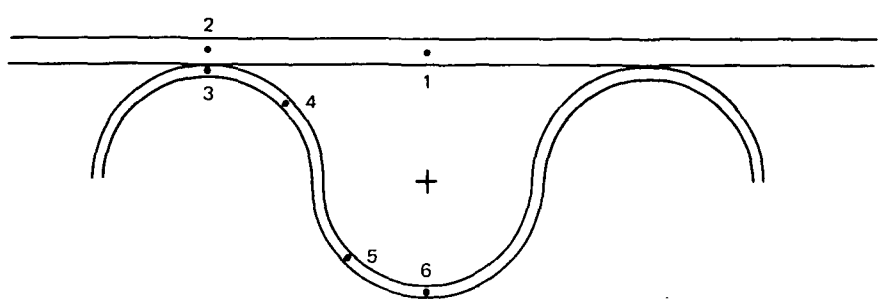

Page Intentionally Left Blank

SECTION 5 THERMAL DYNAMIC TESTING

A practical study into various aspects of testing the model described and analyzed in Sections 3 and 4 was performed. Special consideration and highlights of this effort, as they apply to the physical realization of the hot fin and thermal dynamic model testing in general, are described below.

5.1 METHODS AVAILABLE

For geometrically reduced models made of the same material as the prototype, the discussion of Section 2.1 indicates that the time scale, τ, must shrink in exactly the same ratio as the linear dimension scale, λ, for problems in which radiation is the dominant mode of internal heat transfer. Thus, to simulate fin heating associated with reentry, a 1/10th scale model would have to achieve the same temperature levels in a time span of the order of three minutes. Thus, the structural properties will be changing rapidly. As possible solutions to the problems this introduces, a number of techniques for obtaining natural vibration frequencies and mode shapes during a short time span are presented.

5.1.1 Single Mode Methods

Two mode-by-mode procedures to obtain natural vibration frequencies and mode shapes during transient heating are presented in References 12 and 13. The methods discussed attempt to electronically track a single mode as its frequency varies (due to transient heating) by means of a servo control which constantly adjusts the input frequency to maintain the system in resonance. Depending upon the type of electronic circuitry employed, the control systems which have been used respond to either peak amplitude or phase angle. A third approach used in this family of single mode methods employs a fixed excitation frequency during heating, while the output instrumentation records the precise instant when the system is in resonance at the applied forcing frequency. Needless to say, these test procedures require many repeated applications of the thermal duty-cycle to track a reasonable number of structural modes, as well as the servo electronics to effect the desired control.

5.1.2 Multimode Methods

Alternate and potentially very attractive procedures for determining frequencies and mode shapes of structures with rapidly changing properties involve the processing of transient data to obtain steady-state information. The main differences among the various methods, as will be seen, is in the type of structural dynamic excitation required.

The "Impulse Response Method" is based upon measuring the response history, $\bar{h}_{ij}(t)$, at various structural locations, i, to an impulse load applied at point j. By comparing the Fourier transformed equations of motion to impulsively loaded structures with those for sinusoidal excitation, it can be shown that a complex frequency response at point i, $H_{ij}(\omega)$, caused by steady-state vibration excitation applied at j, may be calculated from the relationship

$$H_{ij}(\omega) = \int_{-\infty}^{\infty} \bar{h}_{ij}(t)\, e^{-i\omega t}\, dt$$

Thus, H_{ij} may be evaluated numerically once the $\bar{h}_{ij}$ are determined from recorded experimental data. For lightly damped structures with reasonably spaced frequencies, natural frequencies and mode shapes may be extracted from these calculations since

$$\left\{\phi_i^{(k)}\right\} \simeq \left\{H_{ij}(\omega_k)\right\}$$

where $\left\{\phi_i^{(k)}\right\}$ is the modal vector corresponding to the kth natural frequency, ω_k.

A number of practical aspects associated with implementation of this method have been investigated and documented in a series of reports issuing from the University of Southampton (References 14 through 16) and Grumman Aerospace (References 17 through 19). Problems associated with excitation level and duration, length of recorded output data, closely spaced natural frequencies and data reduction using proper filtering and interpretation techniques, are discussed in these works with reference to tests actually performed.

The testing procedure used in the "Rapid Frequency Sweep Method" is to load the structure by a constant amplitude excitation of rapidly varying frequency (References 14 and 20). The idea behind this is similar to the impulse method in that the Fourier transforms of input and response may be used to compute the complex frequency response obtained from conventional steady-state vibration testing.

Advantages of the rapid frequency technique over the impulse response method are: the input energy can easily be made larger since a longer exicitation time is involved (hence, the output is also larger and less susceptible to measurement and processing error) and the range of resonances excited can be more accurately controlled, thus simplifying the required analogue-to-digital conversion of response data. As compared with steady-state testing techniques, transient tests, such as the impulse response and rapid frequency sweep methods minimize testing time, but greatly increase the data processing task.

The "Step Input Method" is similar to the impulse and rapid frequency sweep test methods in that it uses Fourier transform computations of recorded transient structural responses, except that now the excitation input is a suddenly released static displacement of the structure. This technique was proposed by R. Mazet (Reference 21) and was also used with success by others (References 22 and 23)

5.2 ADDITIONAL TEST CONSIDERATIONS

5.2.1 Heating Inputs

The surface area involved and thermal flow rates required for providing reentry temperatures in the present study are sufficiently large so as to preclude the use of aerodynamic wind tunnel heating. This suggests the use of radiant heating by quartz lamps which are programmed and controlled to deliver desired temperature-time curves over various regions of the structure. Each region is designed to have an attached thermocuple follow a specified temperature history. The problem of heat leakage at boundaries can be overcome by oversized heating elements or by having separate adjacent regions controlled by guard heaters.

Because of the requirement of high temperatures for short times, it is possible that the cooling phase of the curve may be the most difficult to simulate thermally For example, the hot fin skin temperature drops some $500C^{o}$ ($900F^{o}$) in 100 seconds (see Fig. 21). Thus, the test may well require the use of cool air blowers and baffles. In connection with this, it may be desirable to have more precise control elements. A laboratory facility which has a heating power capability of some 500 kva should be adequate for the combination of temperature, mass and thermal rates required for the hot fin.

5.2.2 Instrumentation

The principal types of instruments available for thermal dynamic testing are thermocouples, accelerometers and strain gages. Besides being capable of functioning at elevated temperatures, these instruments should be light-weight, accurate, and capable of withstanding the dynamic environment.

The Ceramo Co. markets a 0.1cm (1/25 in.) OD Chromel-Alummel thermocouple wire with an upper temperature limit of 760°C (1400°F). In addition, it is purported to have a fast response time and a ±3/4% error tolerance. Light-weight electroformed or etched Ni-Cr strain gages which can be welded in place are sold by Microdot Inc. These are conservatively rated for operation up to 510°C (950°F) but have been reported for use in environments of 680°C (1250°F). In addition, Microdot also makes a platinum tungsten weldable alloy strain gage for dynamic measurements up to 815°C (1500°F).

Small and light accelerometers (1.27cm (1/2-in.) OD and 20 gm (0.7 oz), respectively) designed for use at temperatures up to 760°C (1400°F) are produced by Endevco. However, they are expensive (approximately $1,000 each) and, because of their low gain at the temperatures involved, must be operated in conjuction with special charge amplifiers (a possible additional expense). Thus, they should be used more sparingly than strain gages which are much less costly, can be used to obtain comparable natural frequency data and, with some additional effort, may be calibrated to give modal data.

A relatively new method for measuring vibtation of heated structures employs pulsed differential holographic measurements to produce modal interference fringe patterns (References 24 through 26). Although initial acqusition of such a system is costly (somewhere between $50 and $100K) it could provide useful for structural temperature levels in excess of 1100°C (2000°F). In addition, the method is non-contacting and produces entire modal patterns rather than data for a limited number of discrete points.

5.2.3 Mechanical Loading

Long rods or reciprocating arms can be used to transmit loads to specimens in the heating area. These can be connected directly to shakers (Reference 12) and to cam mechanisms designed to deliver an impulse or sudden load-release (References 10 and

22). In many cases, attention must be given to ensure that serious thermal or mechanical distortions are not introduced at the excitation points.

If stiffness measurements during heating are required, or if programmed dynamic loads must be applied simultaneously in the heated area, piezo-electric quartz rods can be used in conjunction with servo control and potentiometers to regulate the mechanical loading with an electric input.

5.2.4 Thermal Cycling

The effects of thermal cycling associated with repeated testing of the specimen should be considered since inelastic deformations might have the effect of changing the structure from test to test. This is most likely to happen in the first few thermal cycles as specimen heating tends to release the manufacturing stresses through deformation associated with material annealing. Since the structures are ordinarly under a 1-g loading only and primary structure materials are normally rather stable, it is expected that the importance of creep phenomena will be small.

5.2.5 Cost Estimates For Testing the Hot Fin

Table 9 lists the man-months and type engineer or technician responsible for each experimental task associated with the hot fin test (cost estimates for model design and manufacture are presented in Section 3.3). Instrumentation charges are additional and are estimated at $2,000 for two high-temperature accelerometers and another $2,000 for thermocouples and high temperature weldable strain gates. Data reduction, involving conversion of analogue tapes to digital data, will require approximately another two man-months of effort.

The experimental program estimates are based upon the following set of experiments: thermal tests without mechanical excitation, dynamic tests at room temperature, and combined thermal-dynamic tests. The unheated dynamic tests were assumed to consist of a frequency sweep and one transient type (i.e. sudden step or impulsive loading test). The purpose of the room temperature dynamic tests will be to provide data for assessment of the thermal dynamic test data through a comparison of transient and steady-state results.

TABLE 9. ESTIMATED MAN-MONTHS FOR TEST OF 1/10th SCALE HOT FIN MODEL

Task \ Responsibility	Thermal Vacuum Test Engineer	Vibration Test Engr	Instru-mentation Engineer	Environ-mental Test Technician	Structural Test Mfg. Technician	Instrumentation Technician
Design holding fixture	1 1/2					
Oversee fabrication of heating array, use of power equipment and test.	1 1/2					
Develop vibration test procedure, oversee setup and mechanical aspects of test.		3				
Acquire thermal and mechanical transducers. Supervise their install-ation and use during test.			4			
Install test article in fixture, locate shakers in place, hook up power and operate equipment during test.				2		
Manufacture thermal vibration holding fixture and assist in test setup.					4	
Install all transducers, connect to recording equip-ment and record instrumen-tation readings during tests.						3
TOTAL (19)	3	3	4	2	4	3

SECTION 6 CONCLUSIONS AND RECOMMENDATIONS

A search of the literature dealing with thermal effects upon dynamic response of engineering structures has uncovered a number of references concerned primarily with either analysis (References 9, 27 and 28) or test (References 10, 22 and 23), but none which correlate the two in a well coordinated and detailed manner. Another observation made, and concurred with in a recent note by Professor Swaim (Reference 29), is that this technical area of investigation was active in the late fifties and early sixties, but very little has since been reported upon. Consequently, there appears to be a need in the shuttle effort to perform concurrent thermal-structural tests and analysis programs and to evolve appropriate confidence levels to be used in evaluating theoretical predictions. Full-scale tests should be performed upon prototype details, such as corrugated skin-stringer attachments and mechanical joints, but larger components such as wings and tails will require the use of reduced scale models. In connection with such experiments, the scaling laws of Section 2 and the instrumentation and test-method information of Section 5 may be of assistance.

Although tests can be performed at room temperature upon models with manufactured reduced stiffness, thus simplifying the need for simultaneously supplying heat and mechanical excitation, such models would be severely restricted, corresponding to only one time instant of a single maneuver. Thus, transient heating tests which simulate an entire environmental phase are preferred.

In connection with such testing, it is felt that thermal scaling errors can be kept small but the possibility of shifting materials and temperature levels is quite impractical because of the number of important variables involved which are temperature dependent. Furthermore, the primary-structure temperature levels are not sufficiently high nor are the dynamic test techniques so difficult that they cannot be adequately managed in an acceptable modeling program with state-of-the-art instrumentation.

Because of the high level of complexity and cost associated with reduced-scale replica models (witness the results of the manufacturing cost study upon the hot fin presented in Section 3) "adequate" thermal-dynamic models, rather than true-replica reduced scaled models, are recommended where possible. Of course this tack requires

an a priori knowledge of the basic parameters, since it assumes that unanticipated problems will not occur. If such phenomena did occur, they could adversely affect the overall stiffness modeling of a non-replica component in a way which did not correlate with behavior of the prototype. For example, if the linear bending to twisting stiffness ratios were identical in model and prototype, i.e.,

$$\frac{\overline{EI}}{\overline{GJ}} = \frac{\overline{(EI)}'}{\overline{(GJ)}'}$$

but thermal stresses caused an unanticipated buckle in a reinforced cover skin (in either model or prototype but not both), the true stiffness ratios would not agree. A replica model would not have this deficiency since nonlinear phenomena which are strain or stress dependent (e.g., buckling), but not time dependent (e.g. creep), would scale one to one.

SECTION 7

REFERENCES

1. Bridgman, P. W.: Dimensional Analysis, Yale University Press, New Haven, Conn., 1931.
2. Langhaar, H. L.: Dimensional Analysis and Theory of Models, John Wiley and Sons, Inc., New York, 1951.
3. Katzoff, S.: "Similitude in Thermal Models of Spacecraft, "NASA TND-1631, April 1963.
4. Dugundji, J.; and Calligeros, J. M.: "Similarity Laws for Aerothermoelastic Testing," JAS, Aug. 1962 (pp 935-950).
5. Land, N. S., "A Compilation of Nondimensional Numbers," NASA SP-274, 1972.
6. Grimes, P. J.; McTigue, L. D.; Riley, G. F.; and Tilden, D. I.: "Advancements in Structural Dynamic Technology Resulting from Saturn V Programs," NASA CR-1540, June 1970.
7. Dwyer, W. J.; Emerton, R. K.; and Ojalvo, I. U.: "An Automated Procedure for the Optimization of Practical Aerospace Structures," Vol. I AFFDL-TR-70-118, April 1971.
8. Leadbetter, S. A.; Leonard, H. W.; and Brock, E. J., Jr.: "Design and Fabrication Considerations for a 1/10 Scale Replica Model of the Apollo/Saturn V," NASA TN D-4138, October 1967.
9. Budiansky, B.; and Mayers, J.: "Influence of Aerodynamic Heating on the Effective Torsional Stiffness of Thin Wings," JAS, Dec. 1956 (pp 1081-1108).
10. McWithey, R. R.; and Vosteen, L. F.: "Effects of Transient Heating on the Vibration Frequencies of a Prototype of the X-15 Wing", TN D-362, 1960.
11. Bruhn, E. F.: Analysis and Design of Flight Vehicle Structures, Tri-State Offset Co, Cincinnati, Ohio (1965).
12. McIntyre, K. L.: "Vibration Testing During High Heat Rates", Proceedings of Symposium on Aeroelastic and Dynamic Modeling Technology, RTD-AIA, Dayton, Ohio, Sept. 1963.
13. Skingle, C. W.: "A Vibration Control System for Resonance Following which Maintains a Pre-Selected Phase Angle Between the Excitation Force and Displacement of the Structure," Royal Aircraft Establishment TN No. Structures 3110, 1963.

14. White, R. G.: "Measurement of Structural Frequency Response by Transient Excitation," Institute of Sound and Vibration Research, Tech Report 12, January 1969.

15. White, R. G.: "Use of Transient Excitation in the Dynamic Analysis of Structures," The Aeronautical Journal of the Royal Aeronautical Society, Vol. 73, pp. 1047-1050, December 1969.

16. White, R. G.: "The Resolution of Close Natural Frequencies in the Impulse Response and Severe Truncation Effects," Institute of Sound and Vibration Research, Tech Report 17, June 1969.

17. Goldenberg, S.; and Cary, J. W.: "An Analytical Method for Predicting the Dynamic Response of a Structure from Experimentally Determined Impulse Transfer Functions," Grumman Report No. 000-SM-010, June 1967.

18. Skipala, R.; Birs, C.; and Schnee, M.: "Results of Impulse Testing of LTA-3 Phase-3 Phase 1B," Grumman Report No. LTF-993-10002, December 1969.

19. M. Mantus: "Development and Evaluation of the Impulse Transfer Function Technique," NASA CR-112025, January 1972.

20. Skingle, C. W.: "A Method for Analyzing the Response of a Resonant System to a Rapid Frequency Sweep Input," RAE Tech. Report 66379, December 1966.

21. Mazet, R.: "Some Aspects of Ground and Flight Vibration Tests," AGARD Report 40-T, April 1956.

22. Lenk, E. J.: "A Method of Measuring Normal Modes and Frequencies with Application to Heated Structures," U. S. Naval Air Engineering Center Report No. NAEC-ASL-1059, 16 May 1963.

23. Grady, G. E.; and Friedman, R.: "Development of a Resonance-Following System for Vibration Testing at Elevated Temperatures," Aeronautical Structures Laboratory Report No. NAMATCEN-ASL-1037, 2 Nov. 1960.

24. R. Aprahamian; and Evensen, D. A.: "Vibration Analysis by Differential Holographic Interferometry," AIAA Journal, Vol. 9, No. 1, January 1971, pp. 186-188.

25. R. Aprahamian; Evensen, D. A.; Mixson, J. S.; and Wright, J. E.: "Application of Pulsed Holographic Interferometry to the Measurement of Propagating Transverse Waves in Beams," Experimental Mechanics, J. Soc. for Experimental Stress Analysis, July 1971, pp. 309-314.

26. Evensen, D. A.; Aprahamian, R., Overoye, K. R.: "Pulsed Differential Holographic Measurements of Vibration Modes of High-Temperature Panels," NASA CR-2028, 1972.

27. Biot, M. A.: "Influence of Thermal Stresses on the Aeroelastic Stability of Supersonic Wings", Journal of Aeronautical Sciences, Vol. 24, No. 6, June 1957, pp. 418-420.

28. Heldenfels, R. R.; and Vosteen, L. F.: "Approximate Analysis of Effects of Large Deflections and Initial Twist on Torsional Stiffness of a Cantilever Plate subjected to Thermal Stresses", NACA Report 1361, 1958.

29. Swaim, R. L.: "Thermal Effects on Aircraft Elastic Mode Shapes," Journal of Aircraft, July-August 1970, p. 379.

Page Intentionally Left Blank

APPENDIX

THERMAL DYNAMIC SCALING LAWS FOR A BEAM

The governing equation for transverse beam vibrations under the influence of heating and axial loading is

$$\frac{\partial^2}{\partial x^2}\left[\overline{EI}\ \frac{\partial^2 w}{\partial x^2} - M_T\right] + \frac{\partial}{\partial x}\left[(\overline{EA}\ \epsilon_x - N_T)\ \frac{\partial w}{\partial x}\right] = \overline{\rho A}\ \frac{\partial^2 w}{\partial t^2}$$

where w is the transverse beam deflection, z and x are the transverse and axial beam coordinates, E, A and ρ are the beams elastic modulus, area and mass density, respectively, and t is time. The remaining variables are defined below.

$M_T = \int E\,\alpha z T\,dA$	"thermal moment"
$N_T = \int E\,\alpha T\,dA$	"thermal force"
$\overline{EI} = \int E\,z^2\,dA$	bending stiffness
$\overline{EA} = \int E\,dA$	stretching stiffness
$\overline{\rho A} = \int \rho\,dA$	mass per unit length
$\epsilon_x = \frac{\partial u}{\partial x} + \frac{1}{2}\left(\frac{\partial w}{\partial x}\right)^2$	strain displacement relationship

where u is the centroid's axial deflection, ϵ_x is the axial strain and α is the coefficient of thermal expansion.

An additional assumption required in the derivation of the vibration equation involves definition of the beam centroid (at each temperature state) which is defined by

$$\int E\,z\,dA = 0$$

Introducing the scaling parameters,

$$\lambda_x = \frac{x'}{x} \qquad \lambda_u = \frac{u'}{u}$$

$$\lambda_z = \frac{z'}{z} \qquad \lambda_w = \frac{w'}{w}$$

$$\lambda_A^2 = \frac{A'}{A} \qquad \frac{T'}{T} = \theta$$

$$\tau_D = \frac{t'}{t}$$

where the primed and unprimed quantities relate to the model and prototype, respectively Substituting the above equations into the nonlinear strain-displacement relationship for the model, yields

$$\epsilon'_x = \frac{\lambda_u}{\lambda_x}\left[\frac{\partial u}{\partial x} + \frac{1}{2}\frac{\lambda_w^2}{\lambda_x \lambda_u}\left(\frac{\partial w}{\partial x}\right)^2\right]$$

Recognizing that it is desirable to have the model strain, ϵ'_x, proportional to the prototype strain, yields

$$\frac{\lambda_u}{\lambda_x} = \left(\frac{\lambda_w}{\lambda_x}\right)^2$$

Thus, $\epsilon'_x = \frac{\lambda_u}{\lambda_x}\epsilon_x$ and the remaining auxiliary scaling laws become

$$\frac{M'_T}{E'\alpha'T'} = \frac{M_T}{E\alpha T}\lambda_z^2\lambda_A^2 \qquad \frac{\overline{EI}'}{E'} = \frac{\overline{EI}}{E}\lambda_z^2\lambda_A^2$$

$$\frac{N'_T}{E'\alpha'T'} = \frac{N_T}{E\alpha T}\lambda_A^2 \qquad \frac{\overline{\rho A}'}{\rho'} = \frac{\overline{\rho A}}{\rho}\lambda_A^2$$

The main scaling laws reduce to

$$\alpha = \alpha\theta\left(\frac{\lambda_x}{\lambda_z}\right)^2 \quad \text{and} \quad \tau_D = \frac{\lambda_x^2}{\lambda_z}\sqrt{\frac{\rho'/E'}{\rho/E}}$$

where

$$\lambda_z = \lambda_w = \lambda_u = \lambda_z^2/\lambda_x$$

It should be noted that axial vibration effects have been ignored in the above derivation. If they were included, the last set of equations would result in

$$\lambda_z = \lambda_x = \lambda, \qquad \alpha\theta = \alpha \text{ and } \tau_D = \lambda\sqrt{\frac{\rho'/E'}{\rho/E}}$$

NATIONAL AERONAUTICS AND SPACE ADMINISTRATION
WASHINGTON, D.C. 20546

OFFICIAL BUSINESS
PENALTY FOR PRIVATE USE $300

SPECIAL FOURTH-CLASS RATE BOOK

POSTAGE AND FEES PAID
NATIONAL AERONAUTICS AND SPACE ADMINISTRATION
451

U.S.MAIL

POSTMASTER: If Undeliverable (Section 158 Postal Manual) Do Not Return

"The aeronautical and space activities of the United States shall be conducted so as to contribute . . . to the expansion of human knowledge of phenomena in the atmosphere and space. The Administration shall provide for the widest practicable and appropriate dissemination of information concerning its activities and the results thereof."

—NATIONAL AERONAUTICS AND SPACE ACT OF 1958

NASA SCIENTIFIC AND TECHNICAL PUBLICATIONS

TECHNICAL REPORTS: Scientific and technical information considered important, complete, and a lasting contribution to existing knowledge.

TECHNICAL NOTES: Information less broad in scope but nevertheless of importance as a contribution to existing knowledge.

TECHNICAL MEMORANDUMS: Information receiving limited distribution because of preliminary data, security classification, or other reasons. Also includes conference proceedings with either limited or unlimited distribution.

CONTRACTOR REPORTS: Scientific and technical information generated under a NASA contract or grant and considered an important contribution to existing knowledge.

TECHNICAL TRANSLATIONS: Information published in a foreign language considered to merit NASA distribution in English.

SPECIAL PUBLICATIONS: Information derived from or of value to NASA activities. Publications include final reports of major projects, monographs, data compilations, handbooks, sourcebooks, and special bibliographies.

TECHNOLOGY UTILIZATION PUBLICATIONS: Information on technology used by NASA that may be of particular interest in commercial and other non-aerospace applications. Publications include Tech Briefs, Technology Utilization Reports and Technology Surveys.

Details on the availability of these publications may be obtained from:

SCIENTIFIC AND TECHNICAL INFORMATION OFFICE

NATIONAL AERONAUTICS AND SPACE ADMINISTRATION

Washington, D.C. 20546